

Water Resources Research

L

RESEARCH ARTICLE

10.1029/2024WR038282

Key Points:

- Open-channel flows through arrays of boulders at the relative submergence (k) ranging from 0.25 to 3.5 is investigated by large eddy simulations
- Three distinct types of coherent structures are identified: (a) near-bed hairpin vortex, (b) lateral flapping of boulder wakes, and (c) meandering of high-speed streaks
- A region of low bed shear stress occurs upstream of boulders at low k while this region is present in the wake of boulders at high k, justifying the deposition patterns depending on k as shown by Papanicolaou et al. (2018, https://doi.org/10.1029/2018jf004753)

Supporting Information:

Supporting Information may be found in the online version of this article.

Correspondence to:

Y. Liu and H. Fang, liuy8@sustech.edu.cn; fanghw@tsinghua.edu.cn

Citation:

Tang, Z., Stoesser, T., Huang, L., Liu, Y., & Fang, H. (2025). Impact of the relative submergence on turbulence structures in open-channel flow through arrays of large spherical roughness elements. *Water Resources Research*, *61*, e2024WR038282. https://doi.org/10.1029/2024WR038282

Received 8 AUG 2024 Accepted 7 MAY 2025

Author Contributions:

Formal analysis: Zhengdao Tang Funding acquisition: Yan Liu, Hongwei Fang Investigation: Zhengdao Tang Methodology: Thorsten Stoesser, Yan Liu Supervision: Thorsten Stoesser, Lei Huang, Hongwei Fang

Validation: Zhengdao Tang Writing – original draft: Zhengdao Tang

© 2025 The Author(s).

This is an open access article under the terms of the Creative Commons

Attribution-NonCommercial License, which permits use, distribution and reproduction in any medium, provided the original work is properly cited and is not used for commercial purposes.

Impact of the Relative Submergence on Turbulence Structures in Open-Channel Flow Through Arrays of Large Spherical Roughness Elements

Zhengdao Tang¹, Thorsten Stoesser², Lei Huang³, Yan Liu¹, and Hongwei Fang^{3,4}

¹Department of Environmental Science and Engineering, Southern University of Science and Technology, Shenzhen, China, ²Department of Civil, Environmental and Geomatic Engineering, University College London, London, UK, ³Department of Hydraulic Engineering, Tsinghua University, Beijing, China, ⁴Department of Ocean Science and Engineering, Southern University of Science and Technology, Shenzhen, China

Abstract This study investigates the impact of relative submergence, defined as the ratio of water depth to the diameter of boulders (k = H/D), on turbulence structures in flow through boulder arrays. The large-eddy simulation method is employed to simulate flow through boulder arrays across a range of k values from 0.25 to 3.50. Within this range, three distinct flow regimes are identified: low (k = 0.25), intermediate (k = 0.75) and 1.25), and high (k = 2.0 and 3.5) relative submergence regimes. Across these three regimes, distributions of time-averaged velocities, secondary flow, turbulent kinetic energy, and dominant turbulence structures in the wakes of boulders exhibit significant variations. The wake of boulders, characterized by recirculation flow, only manifests at $k \ge 0.75$ and is more pronounced at higher k values. Particularly at k = 3.5, funnel vortices in the wake and secondary flow at the sides of boulders develop, enhancing vertical momentum exchange. Three types of coherent structures are identified within the wake: (a) the near-bed hairpin vortex with a wavelength (λ) of 0.8D at the lowest k, (b) the lateral flapping of boulder wakes with $\lambda = 2.1D$ intermediate k, and (c) the meandering of high-speed streaks at the side of boulders with $\lambda = 10D$ at high k. These structures alter the distribution of the near-bed Reynolds shear stresses (RSS) and contribute up to 20% of the near-bed RSS. At $k \le 1.25$, a region of low near-bed shear stress appears upstream of boulders, while it shifts to the wake of boulders at k = 3.5, contributing the observed variations in deposition patterns at different k values as reported by Papanicolaou et al. (2018, https://doi.org/10.1029/2018jf004753). In addition, the two bedload periodicities reported in the experiment of Papanicolaou et al. (2018, https://doi.org/10.1029/2018jf004753) are justified by the ratio of the wavelength of lateral flapping of boulder wakes to that of meandering of low- and high-speed streaks.

1. Introduction

In mountainous rivers, the riverbed typically comprises clusters of large, relatively stationary boulders interspersed with smaller, more mobile sediments (Bathurst, 1987; Rickenmann, 2001; Tsakiris et al., 2014; Wilcock & Crowe, 2003; Yager et al., 2007). The presence of these large boulders significantly influences the adjacent mean and turbulent flow fields (Dey et al., 2011; Ozgoren et al., 2013; Parker, 2013; Shamloo et al., 2001). Furthermore, the relative submergence (k), defined as the ratio of mean water depth (H) to boulder diameter (D), varies widely due to seasonal fluctuations in flow rates (Polvi, 2021). For instance, Bathurst (2002) conducted a survey of 27 mountainous sites across the UK, USA, and Czech Republic, revealing a relative submergence variation ranging from 0.37 to 11.4. Despite considerable spatiotemporal heterogeneity, the turbulent flow through boulder clusters has attracted considerable attention due to its impacts on sediment erosion and deposition processes (Fang et al., 2017; Kramer & Papanicolaou, 2012; Papanicolaou et al., 2012; Yager et al., 2007), effects on fish habitat (Lacey & Roy, 2008; Shamloo et al., 2001), and the induction of hyporheic exchanges (Dudunake et al., 2020; Lee et al., 2022), among other phenomena.

Extensive investigations have been conducted on mean flow patterns and turbulence structures over fully submerged boulders, resulting in several key findings. These include an S-shaped mean velocity profile downstream of boulders (Ozgoren et al., 2013), an elongated layer of high turbulence intensity and Reynolds shear stresses (RSS) at the boulder crest (Dey et al., 2011; Strom & Papanicolaou, 2007), and the presence of large-scale coherent flow structures such as tip vortices and horseshoe vortices near boulders (Ferro, 2003; Hajimirzaie et al., 2014; Strom & Papanicolaou, 2007; Tsakiris et al., 2014). Additionally, several vortex shedding

TANG ET AL.



Writing - review & editing: Thorsten Stoesser, Yan Liu, Hongwei Fans mechanisms due to boulders have been identified, including a detached shear layer (Best, 2001) and the flapping of the wake (Best, 2001; Hajimirzaie & Buchholz, 2013; Liu et al., 2017).

The majority of these investigations have focused on flow characteristics in regions of high relative submergence (HRS), where k > 3.5 (Kramer & Papanicolaou, 2012). Relatively few studies (Baki et al., 2016; Golpira et al., 2023; Hajimirzaie et al., 2012; Monsalve & Yager, 2017; Shamloo et al., 2001) have delved into the turbulence in low relative submergences (LRS, with k close to 1 or less) due to the complexities involved in accurately capturing free surface fluctuations both numerically and experimentally. Velocity measurements conducted using point probes offer only limited insights, suggesting that reverse flow in LRS flows (k < 1.3) may be stronger than in HRS flows (Shamloo et al., 2001). Recent advancements in particle image velocimetry techniques have enabled a two-dimensional quantitative comparison of mean statistical properties in the wake of boulders at 1.3 < k < 3.0 (Golpira et al., 2023), revealing significantly elevated turbulent kinetic energy (TKE) and RSS at low k. Arguably, the numerical simulation conducted by Monsalve and Yager (2017) represents a pioneering attempt, if not the only one, investigating water-surface effects in LRS flows. They employed the unsteady Reynolds-Averaged Navier-Stokes (RANS) equations and investigated the time-averaged hydrodynamics in the vicinity of boulders. Despite advancements in understanding the mean flow field, there remains a lack of knowledge concerning turbulence structures such as large-scale motions (LSM) near boulders for LRS flows, despite their significant contribution to RSS (Duan et al., 2021).

Several flume experiments have demonstrated significant differences in sediment deposition patterns between low relative submergence (LRS) and HRS flows (Monsalve et al., 2017; Papanicolaou et al., 2018; Polvi, 2021). In flows with HRS (k > 3.5), sediment tends to accumulate downstream of large roughness elements (Papanicolaou et al., 2012, 2018). Conversely, in low relative submergence regimes (k < 3.5), studies have observed the deposition of sediments directly upstream of boulders (Monsalve et al., 2017; Papanicolaou et al., 2018; Polvi, 2021). Monsalve and Yager (2017) attributed the formation of upstream sediment patches to negative shear stress divergence upstream of boulders in LRS flows. However, their use of unsteady RANS models is limited in capturing the amplification of turbulence with complex boundary flows (Kang et al., 2011; Rodi et al., 2013; Tokyay & Constantinescu, 2006). Consequently, the predicted near-bed RSS exceeds the critical shear stress for sediment incipient motion upstream of boulders, where sediment deposition is observed in corresponding flume experiments (Monsalve et al., 2017).

In this study, large-eddy simulations of open-channel flow through boulder arrays are conducted across a range of relative submergences from k = 0.25 to 3.5. The main questions motivating this investigation are as follows: What are the effects of relative submergence on the time-averaged flow field and Reynolds stress near boulders? How does k influence turbulence structures within boulder arrays? Ultimately, how can these findings elucidate the diverse sediment deposition patterns observed under varying k conditions by Papanicolaou et al. (2018)?

2. Numerical Method

2.1. Governing Equations

In this study, the method of large-eddy simulation, using the open-source code Hydro3D, is employed to study the turbulence in open-channel flow through boulder arrays. Hydro3D has been validated and applied to several flows of similar complexity to the one reported here (Liu et al., 2017, 2019, 2022b). The code solves the filtered Navier-Stokes equations for incompressible, unsteady and viscous flow reading:

$$\frac{\partial u_i}{\partial x_i} = 0 \tag{1}$$

$$\frac{\partial u_i}{\partial t} + \frac{\partial u_i u_j}{\partial x_i} = -\frac{1}{\rho} \frac{\partial p}{\partial x_i} + \frac{\partial (2\nu S_{ij})}{\partial x_i} - \frac{\partial \tau_{ij}}{\partial x_i} + f_i + g_i \tag{2}$$

where u_i or u_i is the resolved velocity vector (i or j = 1, 2, and 3 represent x-, y- and z-axis directions, respectively); and similarly, x_i represents the spatial vectors in the three directions; ρ is water density; p is the resolved pressure; ν is the kinematic viscosity; f_i is the volume force introduced in the immersed boundary (IB) method proposed by Uhlmann (2005) to impose the no-slip and impermeable constraints on the fluid-solid interface; g_i is the gravitational acceleration; and S_{ii} is the filtered strain-rate tensor. The sub-grid scale (SGS) stress is defined as

TANG ET AL. 2 of 25

com/doi/10.1029/2024WR038282, Wiley Online Library on [17/07/2025]. See the Terms

 $\tau_{ij} = -2\nu_t S_{ij}$ and the wall-adapting local eddy viscosity (WALE) model proposed by Nicoud and Ducros (1999) is used to model the SGS stress. The calculation formula for the turbulent subgrid scale eddy viscosity of this model is:

$$v_{t} = (C_{\omega}\Delta)^{2} \frac{\left(s_{ij}^{d} s_{ij}^{d}\right)^{\frac{2}{3}}}{\left(S_{ij}S_{ij}\right)^{\frac{5}{2}} + \left(s_{ij}^{d} s_{ij}^{d}\right)^{\frac{5}{4}}} \tag{3}$$

where $C_{\omega} = 0.46$, $\Delta = (\Delta x \Delta y \Delta z)^{\frac{1}{3}}$ the traceless symmetric part of the square of the velocity gradient tensor can be calculated using the following formula:

$$s_{ij}^{d} = \frac{1}{2} (g_{ik}g_{kj} + g_{jk}g_{ki}) - \frac{1}{3}\delta_{ij}g_{kk}^{2}, g_{ij} = \frac{\partial u_{i}}{\partial x_{i}}$$
(4)

The convection and diffusion terms of the Navier-Stokes equations are approximated by fourth-order accurate central differences. An explicit 3-step Runge-Kutta scheme is used to integrate the equations in time, providing second-order accuracy. A fractional step method is employed, that is, within the time step convection and diffusion terms are solved explicitly first in a predictor step which is then followed by a corrector step during which the pressure and divergence-free-velocity fields are obtained via a Poisson equation. The latter is solved iteratively through a multi-grid procedure (Ouro et al., 2019).

The location of the water surface is calculated in every time step using the level-set method (Osher & Sethian, 1988). The method is based on a level-set signed distance function φ and it is formulated as:

$$\varphi(x,t) \begin{cases} <0 \text{ if } x \in \Omega_{\text{gas}} \\ =0 \text{ if } x \in \Gamma \\ >0 \text{ if } x \in \Omega_{\text{liquid}} \end{cases}$$
 (5)

where Ω_{gas} is the air-phase domain, Ω_{liquid} is the water-phase domain and Γ represents the interface. The interface movement is calculated through a pure convection equation:

$$\frac{\partial \varphi}{\partial t} + u \cdot \nabla \varphi = 0 \tag{6}$$

Discontinuities between density and viscosity at the interface can lead to numerical instabilities. This is avoided by setting a transition zone in which density and viscosity transitions between water and air is smoothed.

$$\rho(\varphi) = \rho_g + (\rho_l - \rho_g)H(\varphi)$$

$$\mu(\varphi) = \mu_o + (\mu_l - \mu_o)H(\varphi)$$
(7)

The transition zone is defined as $|\varphi| \le \varepsilon$, where ε is half the thickness of the interface. This is implemented through the Heaviside Function $H(\varphi)$ as formulated:

$$H(\varphi) = \begin{cases} 0 & \text{if } \varphi < -\varepsilon \\ \frac{1}{2} \left[1 + \frac{\varphi}{\varepsilon} + \frac{1}{\pi} \sin\left(\frac{\pi\varphi}{\varepsilon}\right) \right] & \text{if } \varphi \le \varepsilon \\ 1 & \text{if } \varphi > \varepsilon \end{cases}$$
 (8)

Although the level set method is successful in capturing the air-water interface, instabilities can arise if φ does not maintain its property of $|\nabla \varphi| = 1$ as time advances. This is addressed through a re-initialization technique applied in the transition zone. The re-initialized signed distance function d is calculated by solving the partial differential equation given by Sussman, Smereka, and Osher:

TANG ET AL. 3 of 25

19447973, 2025, 6, Downloaded from https://agupubs.onlinelibrary.wiley.com/doi/10.1029/2024WR038282, Wiley Online Library on [17/07/2025]. See the Terms and Conc

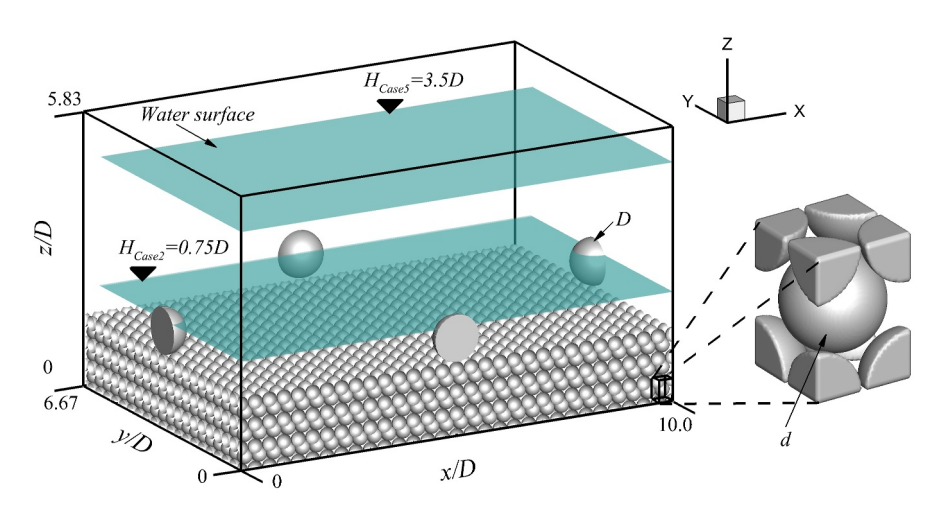


Figure 1. The computational domain of the LES.

$$\frac{\partial d}{\partial t_a} + s(d_0)(|\nabla d| - 1) = 0 \tag{9}$$

where $d_0(x,0) = \varphi(x,t)$, t_a is the artificial time and $s(d_0)$ is the smoothed sign function formulated as:

$$s(d_0) = \frac{d_0}{\sqrt{d_0^2 + (\nabla d_0 | \varepsilon_r)^2}} \tag{10}$$

This partial differential equation is solved for several iteration steps, $\varepsilon_r/\Delta t_a$ where ε_r is a single grid space. These adjustments to the level set method are applied only in the interface zone.

2.2. Computational Setups

Figure 1 illustrates the domain and the setup of the simulations. The channel bed is artificially roughened with seven layers of spheres, each with a diameter of d = 0.0192 m. Four large boulders, each with a diameter of D = 3d = 0.0576 m, are placed diagonally on the top layer of spheres. The bed elevation ($z_{\text{bed}} = 0.091$ m) is defined at the crest of this top layer, and the vertical distance above the riverbed is denoted by z_1 , defined as $z_1 = z - z_{\text{bed}}$. The current bed configuration allows for a 2.3% coverage of large boulders over the total riverbed area, consistent with the boulder concentration in mountainous rivers (1%–34% and 5%–15% of the total riverbed as reported by Montgomery & Buffington, 1997; Nativ et al., 2022, respectively).

Table 1The Hydraulic Parameters for the Six Cases

Case	1	2	3	4	5	6
U_b (m/s)	0.3	0.3	0.3	0.3	0.3	0.78
H(m)	0.0144	0.0432	0.072	0.1152	0.202	0.202
k = H/D	0.25	0.75	1.25	2.0	3.5	3.5
$u_{*,g}/U_b$	0.141	0.181	0.183	0.147	0.125	0.247
$u_{*,bou}/U_b$	0.042	0.042	0.030	0.032	0.029	0.057
$u_{*,sph}/U_b$	0.049	0.045	0.044	0.037	0.034	0.067
Re	4,320	12,960	21,600	34,560	60,600	157,560
Fr	0.798	0.461	0.357	0.282	0.213	0.554

Table 1 provides the details of the simulations in terms of their hydraulic properties. In total, six simulations with different relative submergences are performed. For Cases 1 to 5, the bulk flow velocity is maintained constant, while the relative submergence, defined as the ratio of water depth to boulder diameter (H/D), is increased from k=0.25 to k=3.5. This leads to an increase in the Reynolds number, defined as $\text{Re}=U_bH/\nu$, from 4,320 to 60,600 and a decrease in the Froude number, defined as $\text{Fr}=U_b/\sqrt{gH}$, from 0.80 to 0.21. Case 6 serves as the validation case, based on the flume experiment conducted by Papanicolaou et al. (2012) at k=3.5, the data of which are used to validate the LES. Three types of friction velocity are shown in Table 1, $u_{*,g}$, $u_{*,bou}$, and $u_{*,sph}$. $u_{*,g}$ represents the global-averaged friction velocity defined as $u_{*,g}=\sqrt{-\frac{H}{\rho}\langle \frac{dP}{dx}\rangle}$, where $\langle \frac{dP}{dx}\rangle$ is the time- and spatially averaged pressure gradient that drives the flow. $u_{*,bou}$ and $u_{*,sph}$ are the friction velocity for boulders and for the top layers of bed spheres, respectively, of which the computing methods are provided in Liu et al. (2024).

TANG ET AL. 4 of 25

19447973, 2025, 6, Downloaded from https://agupubs.onlinelibrary.wiley.com/doi/10.1029/2024WR038282, Wiley Online Library on [17/07/2025]. See the Term

tions) on Wiley Online Library for rules of use; OA articles

 Table 2

 The Domain Sizes and the Meshes for the Six Cases

Case	$rac{L_x}{D},rac{L_y}{D},rac{L_z}{D}$	$\frac{\Delta x}{D} = \frac{\Delta y}{D} = \frac{\Delta z}{D}$	$\Delta x^+, \Delta y^+, \Delta z^+$	ΔD^+	Δd^+
1	10, 6.67, 2.50	1/58	21.2, 21.2, 21.2	5.55	6.27
2	10, 6.67, 3.33	1/58	27.2, 27.2, 27.2	5.52	5.77
3	10, 6.67, 3.33	1/58	27.5, 27.5, 27.5	3.99	5.60
4	10, 6.67, 4.17	1/58	22.1, 22.1, 22.1	4.21	4.70
5	10, 6.67, 5.83	1/58	18.8, 18.8, 18.8	3.85	4.30
6	10, 6.67, 5.83	1/58	29.6, 29.6, 29.6	7.58	5.77

Periodic boundary conditions are applied in the streamwise and spanwise directions. A no-slip boundary condition is applied at the channel bottom, and the water surface deformation is calculated by the LSM, as described in the previous section. Additionally, no-slip boundary conditions are applied at the surfaces of bed spheres and large boulders using the direct force immersion boundary method proposed by Uhlmann (2005).

Table 2 provides the domain sizes and meshes used for the simulations. The computational domain, in terms of large boulder diameter, spans $L_x = 10D$ in the streamwise direction and $L_y = 6.67D$ in the spanwise direction. The computational domain height, L_z , for the six cases varies from 2.5D at k = 0.25 in Case 1 to 5.83D at k = 3.5 in Cases 5 and 6. This setup allows for a placement of an approximately 0.8D thick air above the water surface, as required by the LSM. The mesh spacing, in terms of the boulder diameter, is $\Delta x = \Delta y = \Delta z = 1/58D$. Therefore, the grid points in the streamwise and spanwise directions are $N_x = 576$ and $N_y = 384$, respectively. The number of grid points in the vertical direction increases at higher k, ranging from $N_z = 144$ in Case 1 to $N_z = 336$ in Cases 5 and 6. The grid resolutions in wall units, defined as $\Delta^+ = u_{*,g} \times 0.5 \,\Delta/v$, where v is the dynamic viscosity of water, span from $\Delta x^+ = \Delta y^+ = \Delta z^+ = 21.2$ to 29.6. Grid sensitivity tests were carried out in a previous study by Liu et al. (2017), in which all numerical methods and computational setups were the same as in the current Case 6, except for the grid resolution and the top boundary. Liu et al. (2017) reported that simulation results are grid-independent with a resolution in wall units smaller than $\Delta x^+ = 32$, $\Delta y^+ = 28$, and $\Delta z^+ = 32$, which the current simulations satisfy. In addition, the normalized grid spacings near boulders and spheres are also provided in Table 2. The values of ΔD^+ and Δd^+ range from 3.99 to 7.58. This grid resolution ensures at least one grid point in the viscous sublayer near the boulders and spheres, as required by the IB method applied in this study (Uhlmann, 2005).

All simulations are initially run for 10 flow-throughs (FTs), defined as L_x/U_b , to establish fully developed turbulence and are then continued for another 90.2 FTs to collect turbulence statistics. Velocities and pressure data are recorded at the symmetry plane of y/D = 3.33 and at the horizontal plane of $z_1/D = 0.2$ at a frequency of 10 Hz. Additionally, time series of velocities above each sphere's top crest at $z_1/D = 0.2$ are recorded at a frequency of 500 Hz for further analysis.

3. Results

3.1. Validation

Figure 2 presents profiles of (a) the normalized time-averaged streamwise velocity and (b) the normalized root-mean-square streamwise turbulence intensity at selected locations in Case 6. The experimental data, along with the LES results employing a rigid-lid top boundary (LES-Rigid) as published in Liu et al. (2017), are included for comparative analysis. Overall, both simulations demonstrate good agreement with the experimental data, revealing a distinct boulder wake of low streamwise velocity near the bed. Furthermore, the current LES-LSM shows improved agreement with the experimental data near the water surface, where the LES-Rigid overestimates streamwise velocity. The relative error between the average flow velocity obtained using the LES-LSM and LES-Rigid methods and the experimentally measured averaged flow velocity is given in Table S1 in Supporting Information S1. Across all cross-sections, the errors from the LES-LSM method are smaller than those from the LES-Rigid method, except at cross-sections 0 *D* and 7 *D*. The global-averaged relative error for LES-LSM is 4.72%, compared to 6.36% for LES-Rigid, indicating a slight improvement with the application of the level-set method. In terms of the streamwise turbulence intensity, the current LES-LSM demonstrates better

TANG ET AL. 5 of 25

1944/7973, 2025, 6, Downloaded from https://agupubs.onlinelibrary.wiley.com/doi/10.1029/2024WR038282, Wiley Online Library on [17/07/2025]. See the Terms and Conditions (https://onlinelibrary.wiley.com/doi/10.1029/2024WR038282, Wiley Online Library on [17/07/2025]. See the Terms and Conditions (https://onlinelibrary.wiley.com/doi/10.1029/2024WR038282, Wiley Online Library on [17/07/2025]. See the Terms and Conditions (https://onlinelibrary.wiley.com/doi/10.1029/2024WR038282, Wiley Online Library on [17/07/2025]. See the Terms and Conditions (https://onlinelibrary.wiley.com/doi/10.1029/2024WR038282, Wiley Online Library on [17/07/2025]. See the Terms and Conditions (https://onlinelibrary.wiley.com/doi/10.1029/2024WR038282, Wiley Online Library on [17/07/2025]. See the Terms and Conditions (https://onlinelibrary.wiley.com/doi/10.1029/2024WR038282, Wiley Online Library on [17/07/2025]. See the Terms and Conditions (https://onlinelibrary.wiley.com/doi/10.1029/2024WR038282, Wiley Online Library on [17/07/2025]. See the Terms and Conditions (https://onlinelibrary.wiley.com/doi/10.1029/2024WR038282, Wiley Online Library on [17/07/2025]. See the Terms and Conditions (https://onlinelibrary.wiley.com/doi/10.1029/2024WR038282, Wiley Online Library on [17/07/2025]. See the Terms and Conditions (https://onlinelibrary.wiley.com/doi/10.1029/2024WR038282, Wiley Online Library on [17/07/2025]. See the Terms of the T

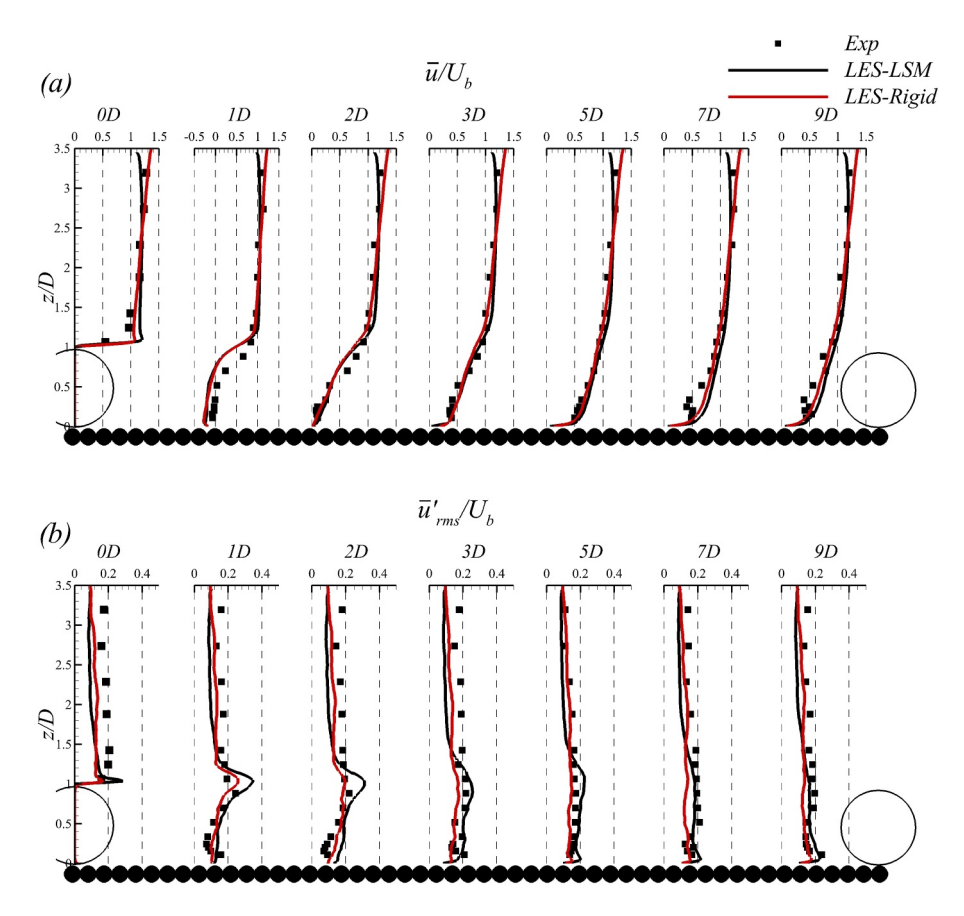


Figure 2. Profiles of (a) the normalized time-averaged streamwise velocity, u/U_b , and (b) the normalized root-mean-square streamwise turbulence intensity, u'_{rms}/U_b , at various locations in the symmetric plane, y/D = 3.33, for Case 6. Experimental data and the LES results with a rigid-lid top boundary taken from Liu et al. (2017) are included as Exp and LES-Rigid for comparison.

agreement near the bed surface at x = 3-9 D than the rigid lid counterpart. This suggests that the use of LSM and hence an accurate representation of local water surface deformations, improves the reproduction of near-bed turbulence structures.

3.2. Impact of k on the Time-Averaged Flow Field

Figure 3 presents contours of the time-averaged streamwise velocity (left column) and vertical velocity (right column) in the symmetry plane for Case 1 (a, b) to Case 5 (i, j). The solid and dashed lines represent the time-averaged water surface and the iso-lines of $\overline{U}/U_b=0.0$, respectively. The lowest streamwise velocities are observed in the wake of boulders, where recirculation regions of length $x/D\approx 2$ form for $k\geq 0.75$ and are absent at k=0.25. The so-called "velocity dip" phenomenon, where the location of the maximum streamwise velocity occurs below the water surface, is observed at the location x/D=8.5, 7.2, and 6.9 for Cases 1, 2, 3, respectively. This "velocity dip" is caused by the momentum exchange at the intermediate water depth due to lateral flapping (shown later in Figures 4 and 11). In Cases 4 and 5, flow above the boulder crest is rarely influenced, maintaining a higher streamwise velocity compared to below the crest.

Contours of the vertical velocity in the right column of Figure 3 indicate strong upward and downward flow at the upstream edge of boulders near the water surface or in the boulder-sphere interspace, respectively. In the near-bed region of the boulder wakes, positive vertical velocities dominate for Cases 2 to 5, whereas no significant vertical velocity presents for Case 1. In Case 3, this upwelling flow interacts with the water surface, generating a local water surface hump at $x/D \approx 1.0$ and two water surface dips upstream or downstream, respectively. In Cases 4 and 5, negative vertical velocities occur at 1.0 < x/D < 3.0, suggesting a flow recirculation in this symmetry plane.

TANG ET AL. 6 of 25

1944/973, 2025, 6, Downloaded from https://agupubs.onlinelibrary.viely.com/doi/10.1029/2024WR038282, Wiley Online Library on [17/07/2025], See the Terms and Conditions (https://onlinelibrary.wiley.com/terms-and-conditions) on Wiley Online Library for rules of use; OA articles of use; O

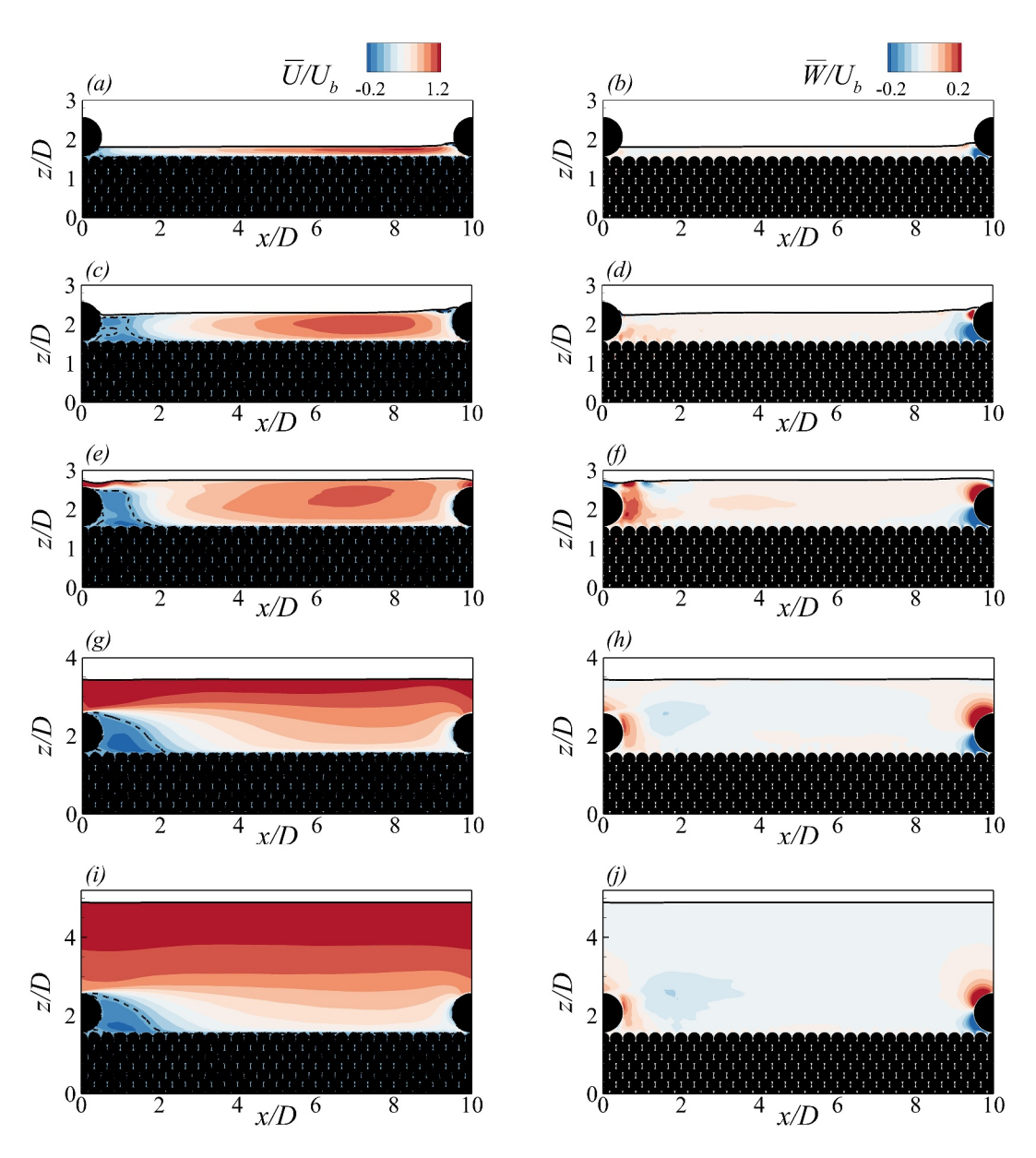


Figure 3. Contours of the time-averaged streamwise velocity (left column) and vertical velocity (right column) in the symmetric plane for Case 1 (a, b) to Case 5 (i, j). The dashed lines in the left column represent the iso-lines of $\overline{U}/U_b = 0$.

The time-averaged streamwise velocity in the cross-section at x/D=1.0 (left column) and x/D=2.0 (right column) for Case 1 (a, b) to Case 5 (i, j) are depicted in Figure 4. The time-averaged secondary flow $(\overline{V}/U_b, \overline{W}/U_b)$ at every tenth points is imposed as black vectors along with a reference arrow in (b). At x/D=1.0, the highest velocity occupies almost the entire water depth at the two sides of the boulders for the three lower k cases, whereas at k=2.0 and 3.5, an apparent boundary layer forms in the near-bed region, with its thickness altered by the pair of secondary flow vortices at the elevation of the boulder crest. This vortex pair spans the whole water depth and transports high-speed fluid from the outer region toward the channel bed where the flow approaches the bed $(y/D \approx 1.0$ and $y/D \approx 6.0$). It dissipates at x/D=2.0 and a spanwise fluid confluence is observed near the channel bed (Figure 4j). Meanwhile, for the three lower k cases, secondary flow at the two sides of boulders primarily displays as spanwise motions of the fluid, with the highest magnitude at intermediate water depths. For example, the spanwise velocity at $y/D=0\sim 2$ (Figures 4c and 4d) is highest at approximately half water depth, enhancing momentum exchange at intermediate elevations and causing the "velocity dip" phenomenon at y/D=0 in Figures 4c and 4d, that is, 3 to 4D upstream of the adjacent boulder (x/D=5.0) and y/D=0.

TANG ET AL. 7 of 25

1944/7973, 2025, 6, Downoladed from https://agupubs.onlinelibrary.wiley.com/doi/10.1029/2024WR083282, Wiley Online Library or [17/07/2025]. See the Terms and Conditions (https://onlinelibrary.wiley.com/doi/10.1029/2024WR083282, Wiley Online Library for rules of use; OA articles of use;

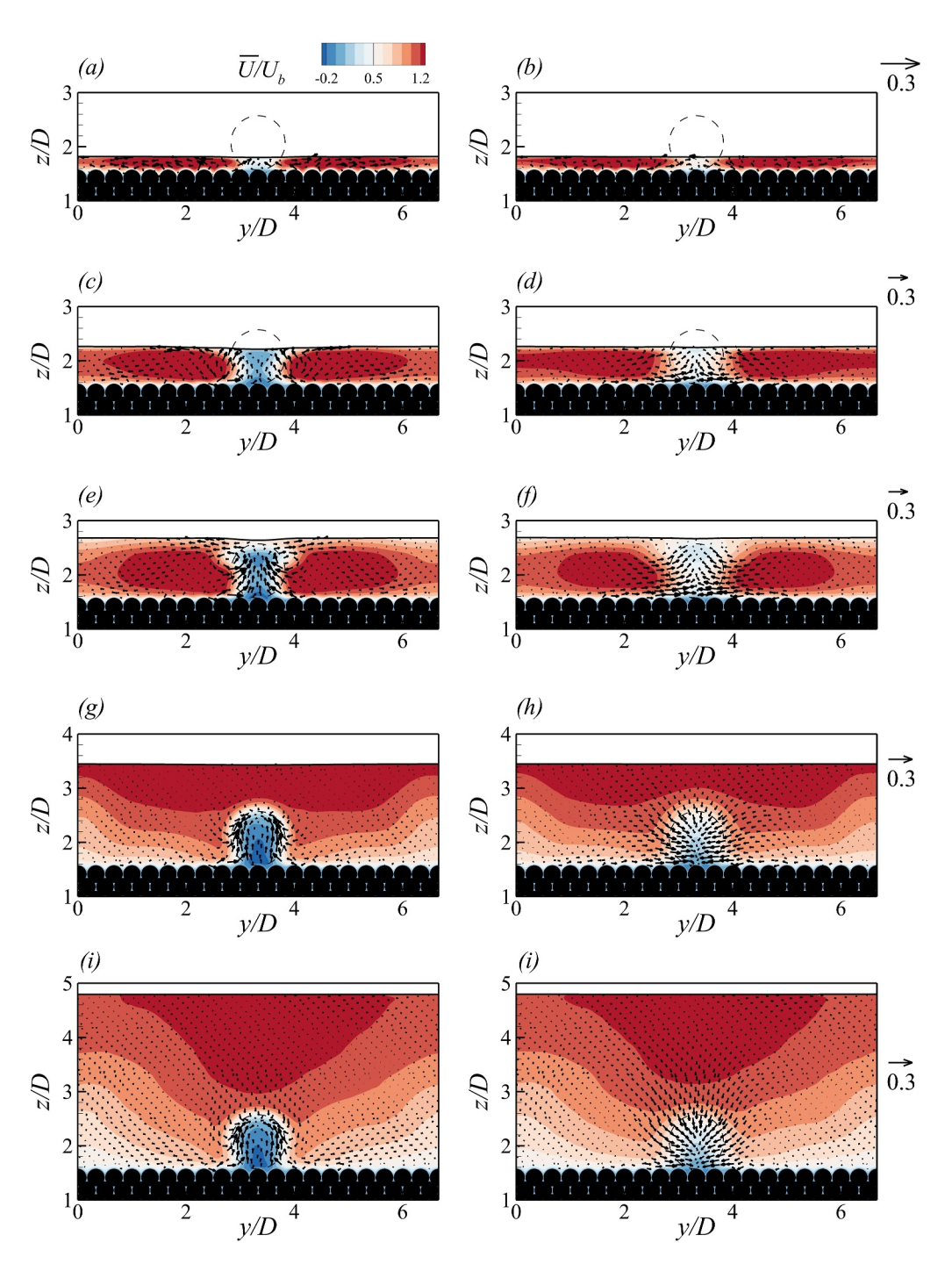


Figure 4. Contours of the time-averaged streamwise velocity in the cross-section at x/D = 1.0 (left column) and x/D = 2.0 (right column) for Case 1 (a, b) to Case 5 (i, j).

Figure 5 illustrates the three-dimensional (3D) streamlines in the wake of boulders for Case 1 (a) to Case 5 (e). The 3D streamlines reveal that flow in the wake of boulders primarily originates from the boulder-sphere interspace for the lowest k (Figure 5a). At k = 0.75 and 1.25, flow at the two sides of the boulder is entrained into the boulder wake due to the strong spanwise velocities observed in Figure 4. At k = 2.0 and 3.5, a tornado-shaped time-averaged wake structure develops in the wake, attracting fluid from the permeable bed and the boulder-sphere interspace into its center (Figures 5d and 5e).

TANG ET AL. 8 of 25

1944 7973, 2025, 6, Downoladed from https://agupubs.onlinelibrary.viley.com/doi/10.1029/2024WR038282, Wiley Online Library on [17/07/2025]. See the Terms and Conditions (https://onlinelibrary.wiley.com/terms-and-conditions) on Wiley Online Library for rules of use; OA articles

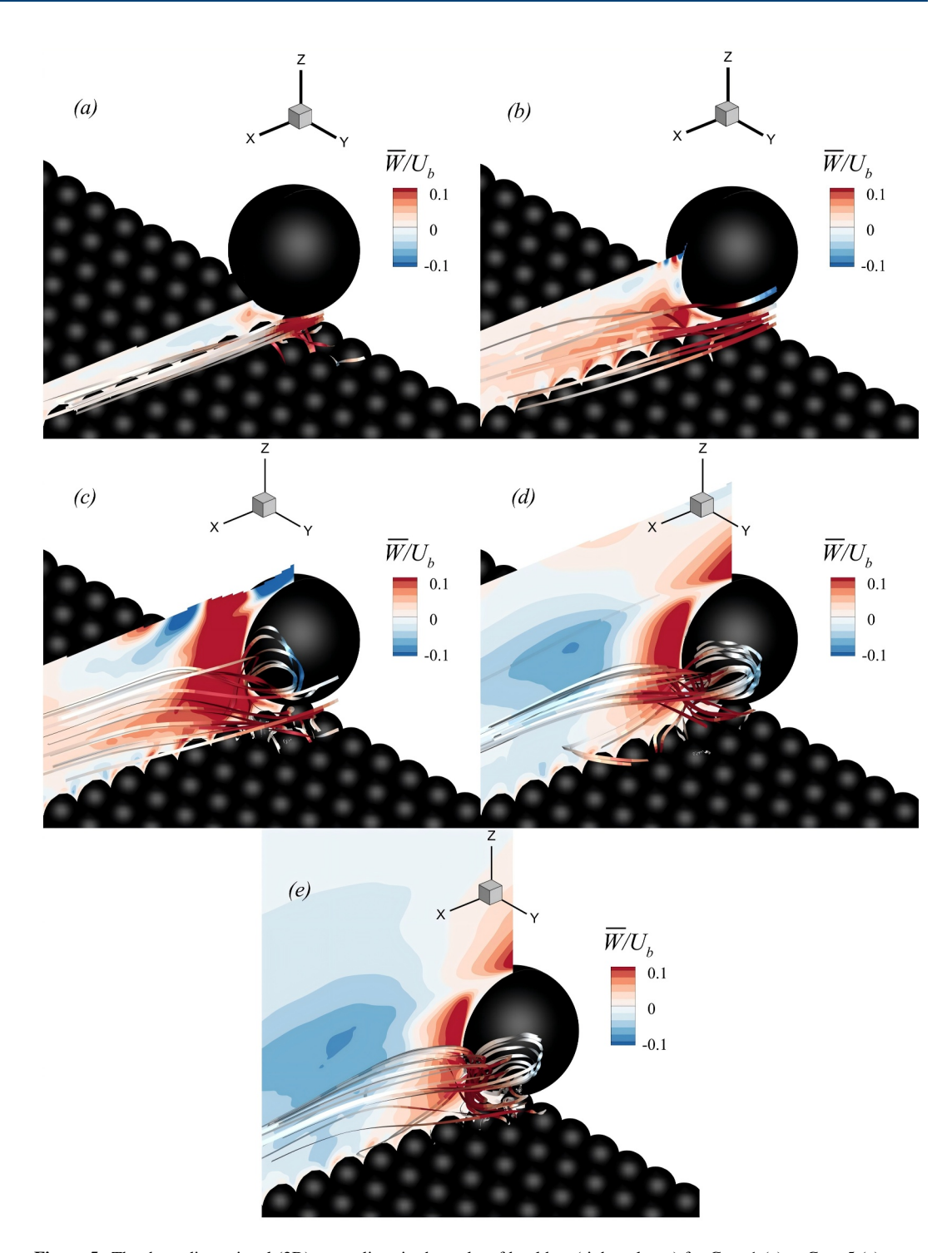


Figure 5. The three-dimensional (3D) streamlines in the wake of boulders (right column) for Case 1 (a) to Case 5 (e).

Contours of the TKE are depicted in Figure 6 in the symmetry plane for Case 1 (a) to Case 5 (e). At k=0.25, TKE displays a uniform distribution across the entire water depth with moderate intensity (TKE/ $u_*^2 \approx 2.0$), except for the region at x/D < 2.0. At k=0.75, a region of high TKE is observed at 1.0 < x/D < 3.0, where the streamwise velocity gradients are the greatest (Figure 3c). At k=2.0 and 3.5, there is an area of high-magnitude TKE just downstream of the crest of the boulder, between the fast-moving fluid over the top of the boulder and the recirculating fluid in the lee of the boulder. Finally, TKE in the case of k=1.25 exhibits transitional features between those in k=0.75 and k=2.0, with high TKE regions observed both in the wake of boulders and

TANG ET AL. 9 of 25

1944/1973. 2025. 6, Downloaded from https://agupubs.onlinelibrary.wiley.com/doi/10.1029/2024WR038282, Wiley Online Library on [17/07/2025]. See the Terms and Conditions (https://onlinelibrary.wiley.com/term

and-conditions) on Wiley Online Library for rules of use; OA articles are governed by the applicable Creative Commons Licenso

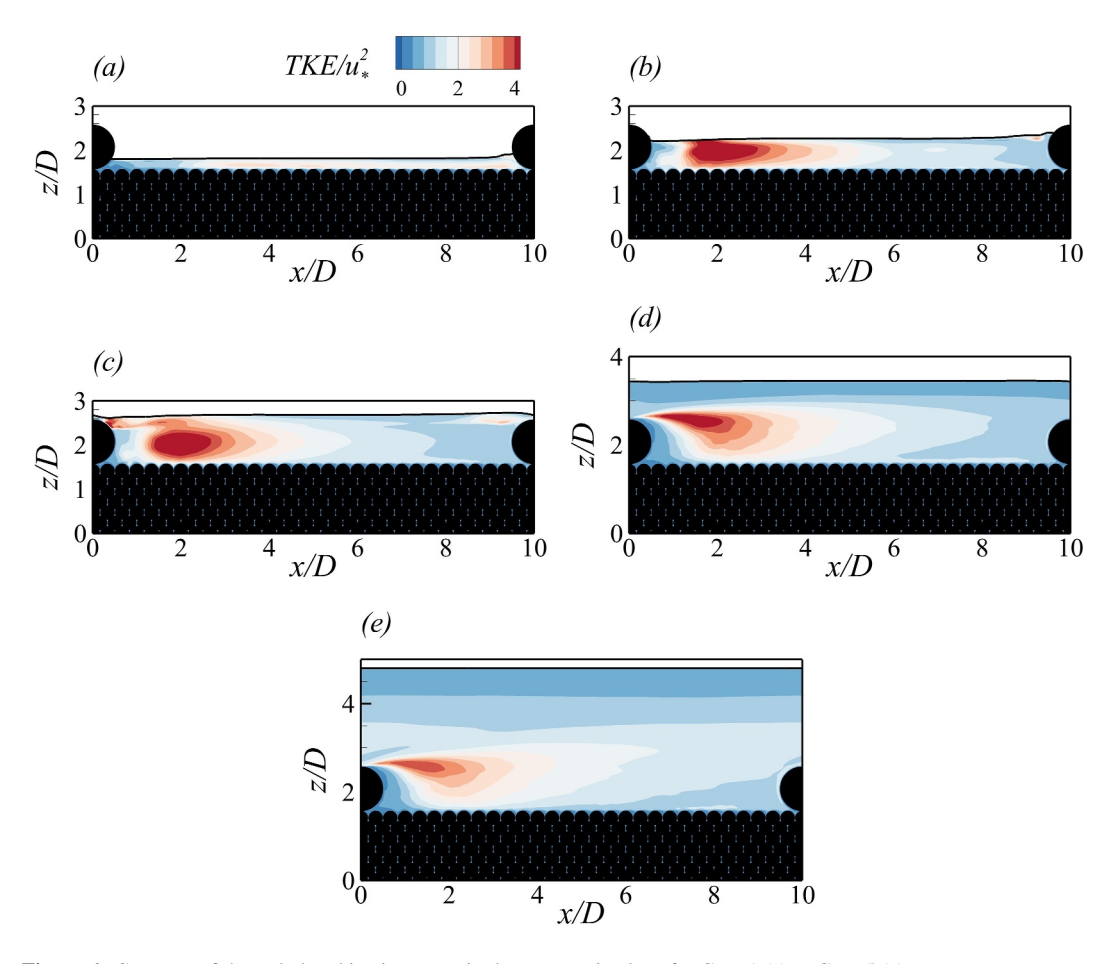


Figure 6. Contours of the turbulent kinetic energy in the symmetric plane for Case 1 (a) to Case 5 (e).

originating from the crest of boulders. Additionally, the magnitude of the highest TKE at k = 0.75 and k = 1.25 is approximately twice of that in the other two cases, indicating stronger turbulence intensities in these two intermediate relative submergence (IRS) regime.

3.3. Turbulence Structures of Different k

Figure 7 presents the coherent structures (CS) visualized by the Q criterion (Q = 1,000) proposed by Hunt et al. (1988), contoured by the distance from the bed surface for Case 1 (a) to Case 5 (e). At k = 0.25, streamwise elongated vortices and hairpin vortices are distributed almost uniformly throughout the domain, except for a meandering streak downstream of boulders where few turbulence structures are observed (Figure 7a). In contrast, at the intermediate k values (k = 0.75 and 1.25), the CS are concentrated in the boulder wakes. Among these CS, the most apparent structures are trains of a spanwise-elongated vortices near the water surface. Additionally, the edges of this high-concentration region exhibit a meandering feature in the streamwise direction. Finally, in Cases 4 and 5, a few streamwise-elongated rollers are observed in the boulder wakes at the elevation of the boulder crest, generated by the shear layer roll-up (Liu et al., 2017). The meandering pattern of the distribution of CS observed in the three lower k cases is absent likely due to the flow recirculation in the vertical direction (Figures 3g and 3i).

In order to further quantify large-scale flow structures, the pre-multiplied spectra (Ps⁺) of the streamwise velocity fluctuation in the symmetry plane at $z_1/D=0.2$ and $x/D=0.5\sim 2.0$ is presented in Figure 8. Four peaks with different wavelengths are observed across all cases: $\lambda=0.8D$ at k=0.25, $\lambda=2.1D$ at $k\leq 1.25$, $\lambda=4.0D$ at k=2.0, and $\lambda=10D$ at $k\geq 2.0$. The $\lambda=0.8D$ peak occurs across all three x/D locations at k=0.25, with the magnitude of $Ps(u)^+$ increasing at higher x/D. This peak also appears at all three x/D locations in the side plane (Figure 9a) where the hairpin vortices of a similar size (0.8D) are observed in Figure 7a. In terms of the $\lambda=2.1D$ peak, it occurs across all three x/D locations at $k\leq 1.25$, with the zenith energy at x/D=1.0 in Case 1 and x/D=2.0

TANG ET AL. 10 of 25

1944 7973, 2025, 6, Downoladed from https://agupubs.onlinelibrary.viley.com/doi/10.1029/2024WR038282, Wiley Online Library on [17/07/2025]. See the Terms and Conditions (https://onlinelibrary.wiley.com/terms-and-conditions) on Wiley Online Library for rules of use; OA articles

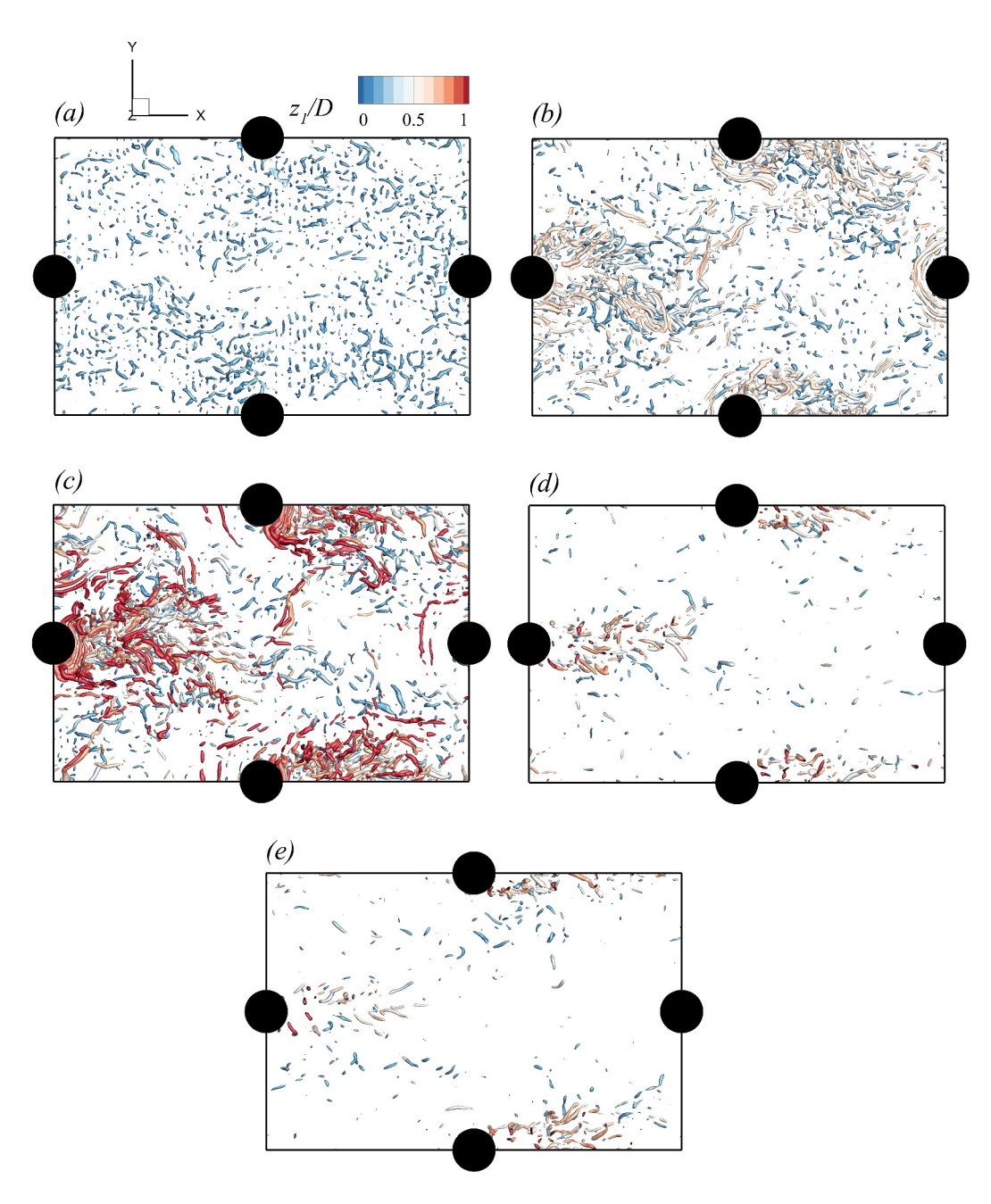


Figure 7. Visualization of the coherent structures by the Q criterion (Q = 1,000) contoured by the distance from the sphere surface for Case 1 (a) to Case 5 (e).

in Cases 2 and 3. In addition, the values of $Ps(u)^+$ equals 2.3 at k=0.75, which is significantly higher than in Cases 1 and 4 ($Ps(u)^+ < 0.6$), explaining the highest TKE regions at x/D=2.0 shown in Figure 6b. This $\lambda=2.1D$ peak corresponds to the lateral flapping of boulder wakes, which is further confirmed by the $Ps(u)^+$ at $z_1/D=0.2$ in the side plane (y/D=3.83) shown in Figure 9. In the three lower k cases, the pre-multiplied spectra in the side plane (Figures 9a–9c) peaks at approximately $\lambda=4.2D$, exactly twice the wavelength of the $Ps(u)^+$ observed in Figures 8a–8c. This is because the symmetry plane receives twice the shed vortices from both sides of the boulder in a single cycle of the flapping of boulders.

At k = 2.0, the pre-multiplied spectra in the symmetry plane peaks at approximately $\lambda = 4.0D$ (Figure 8d), while $Ps(u)^+$ in the side plane peaks at $\lambda = 5.7D$ (Figure 9d). The ratio of these two wavelengths does not indicate any

TANG ET AL. 11 of 25

1947973, 2025, 6, Downloaded from https://agupubs.onlinelibrary.viey.com/doi/10.1029/2024WR032828, Wiley Online Library on [17/07/2025]. See the Terms and Conditions (https://onlinelibrary.viley.com/ems-and-conditions) on Wiley Online Library for rules of use; OA articles are governed by the applicable Creative Commons. Licenseau Conditions (https://onlinelibrary.viley.com/ems-and-conditions) on Wiley Online Library for rules of use; OA articles are governed by the applicable Creative Commons. Licenseau Conditions (https://onlinelibrary.viley.com/ems-and-conditions) on Wiley Online Library for rules of use; OA articles are governed by the applicable Creative Commons. Licenseau Conditions (https://onlinelibrary.viley.com/ems-and-conditions) on Wiley Online Library for rules of use; OA articles are governed by the applicable Creative Commons. Licenseau Conditions (https://onlinelibrary.viley.com/ems-and-conditions) on Wiley Online Library for rules of use; OA articles are governed by the applicable Creative Commons. Licenseau Conditions (https://onlinelibrary.viley.com/ems-and-conditions) on Wiley Online Library for rules of use; OA articles are governed by the applicable Creative Commons. Licenseau Conditions (https://onlinelibrary.viley.com/ems-and-conditions) on Wiley Online Library for rules of use; OA articles are governed by the applicable Creative Commons.

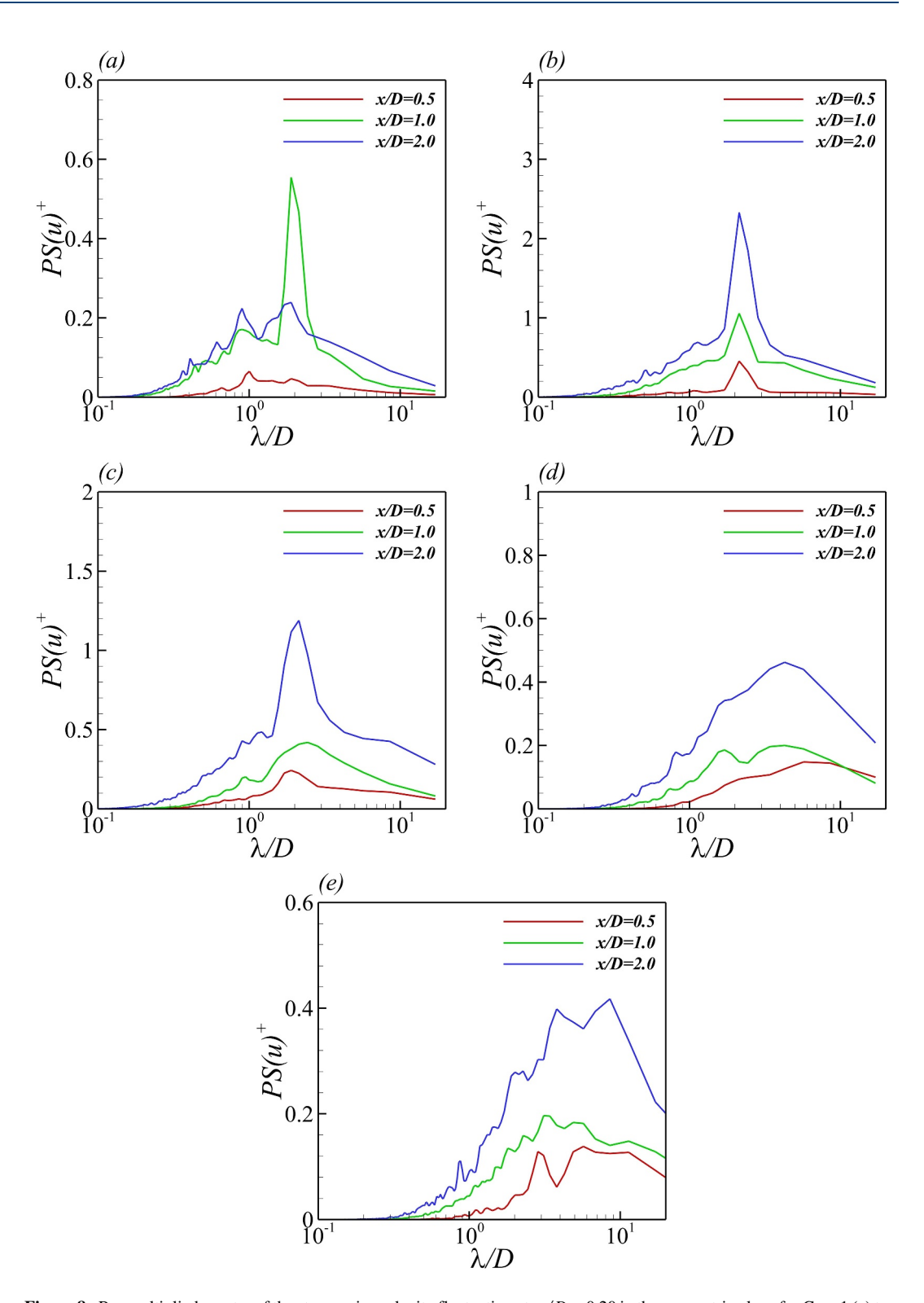


Figure 8. Pre-multiplied spectra of the streamwise velocity fluctuation at $z_1/D = 0.20$ in the symmetric plane for Case 1 (a) to Case 5 (e). The superscript $(\cdot)^+$ represents a normalized quantity by $u_{*,g}^2$.

TANG ET AL. 12 of 25

1944973, 2025, 6, Downloaded from https://agupub.o.nlinelibrary.wiley.com/doi/10.1029/2024WR08282, Wiley Online Library on [17/07/2025]. See the Terms and Conditions (https://onlinelibrary.wiley.com/doi/10.1029/2024WR08282, Wiley Online Library on [17/07/2025]. See the Terms and Conditions (https://onlinelibrary.wiley.com/doi/10.1029/2024WR08282, Wiley Online Library on [17/07/2025]. See the Terms and Conditions (https://onlinelibrary.wiley.com/doi/10.1029/2024WR08282, Wiley Online Library on [17/07/2025]. See the Terms and Conditions (https://onlinelibrary.wiley.com/doi/10.1029/2024WR08282, Wiley Online Library on [17/07/2025]. See the Terms and Conditions (https://onlinelibrary.wiley.com/doi/10.1029/2024WR08282, Wiley Online Library on [17/07/2025]. See the Terms and Conditions (https://onlinelibrary.wiley.com/doi/10.1029/2024WR08282, Wiley Online Library on [17/07/2025]. See the Terms and Conditions (https://onlinelibrary.wiley.com/doi/10.1029/2024WR08282, Wiley Online Library on [17/07/2025]. See the Terms and Conditions (https://onlinelibrary.wiley.com/doi/10.1029/2024WR08282, Wiley Online Library on [17/07/2025]. See the Terms and Conditions (https://onlinelibrary.wiley.com/doi/10.1029/2024WR08282, Wiley Online Library on [17/07/2025]. See the Terms and Conditions (https://onlinelibrary.wiley.com/doi/10.1029/2024WR08282, Wiley Online Library on [17/07/2025]. See the Terms and Conditions (https://onlinelibrary.wiley.com/doi/10.1029/2024WR08282, Wiley Online Library on [17/07/2025]. See the Terms and Conditions (https://onlinelibrary.wiley.com/doi/10.1029/2024WR08282, Wiley Online Library on [17/07/2025]. See the Terms and Conditions (https://onlinelibrary.wiley.com/doi/10.1029/2024WR08282, Wiley Online Library.wiley.com/doi/10.1029/2024WR08282, Wiley Online Library.wiley.com/doi/10.1029/2024WR08282, Wiley Online Library.wiley.com/doi/10.1029/2024WR08282, Wiley Online Library.wiley.com/doi/10.1029/2024WR08282, Wiley Online Library.wiley.wiley.com/doi/10.1029/2024WR08282, Wiley Online Library.wiley.wiley.com

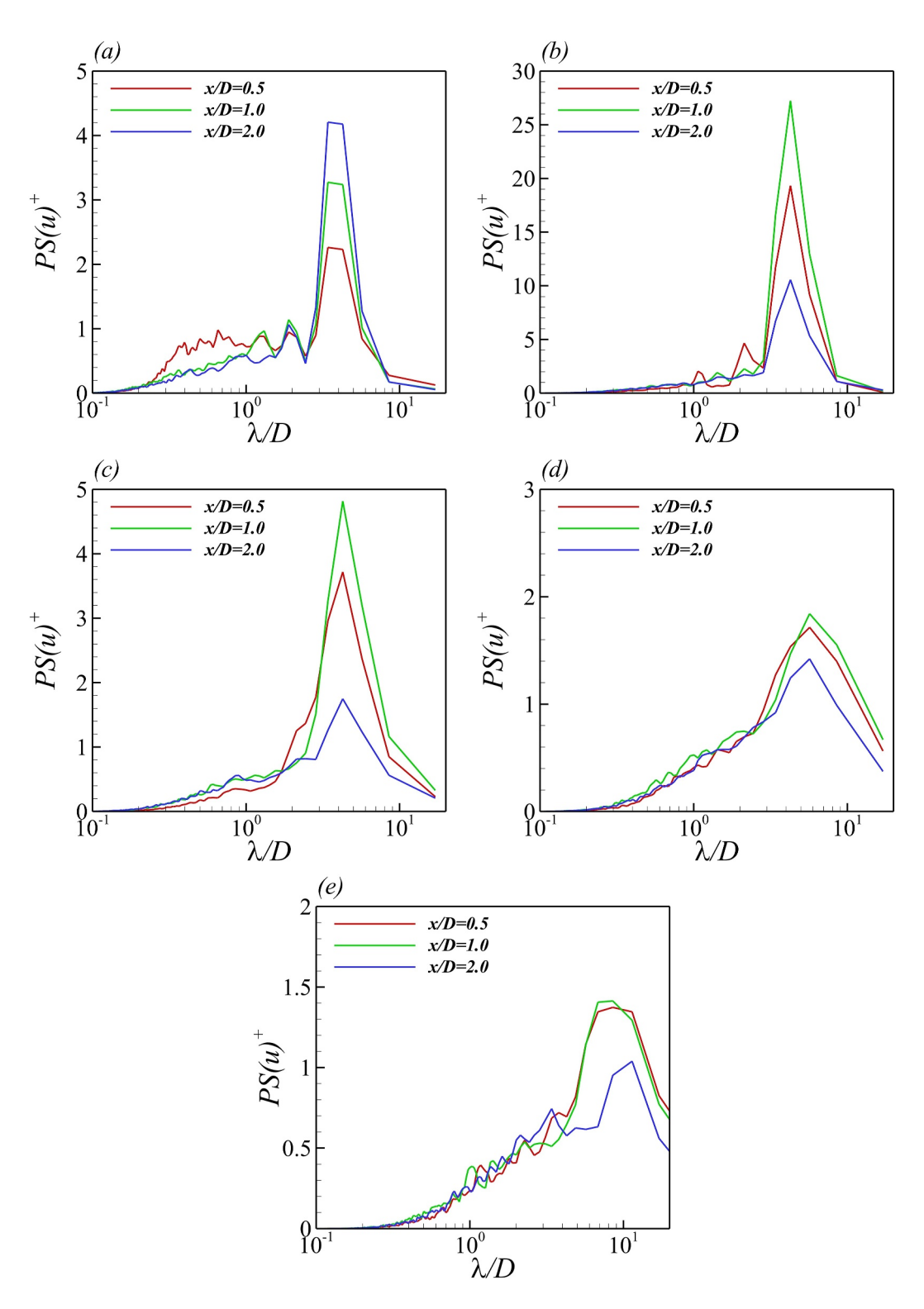


Figure 9. Pre-multiplied spectra of the streamwise velocity fluctuation at $z_1/D = 0.20$ in the plane of y/D = 3.83 for Case 1 (a) to Case 5 (e).

TANG ET AL. 13 of 25

19447973, 2025, 6, Downloaded from https://agupubs.onlinelibrary.wiley.com/doi/10.1029/2024WR038282, Wiley Online Library on [17/07/2025]. See the Terms and Conditions (https://onlinelibrary.wiley.com/doi/10.1029/2024WR038282, Wiley Online Library on [17/07/2025]. See the Terms and Conditions (https://onlinelibrary.wiley.com/doi/10.1029/2024WR038282, Wiley Online Library on [17/07/2025]. See the Terms and Conditions (https://onlinelibrary.wiley.com/doi/10.1029/2024WR038282, Wiley Online Library on [17/07/2025]. See the Terms and Conditions (https://onlinelibrary.wiley.com/doi/10.1029/2024WR038282, Wiley Online Library on [17/07/2025]. See the Terms and Conditions (https://onlinelibrary.wiley.com/doi/10.1029/2024WR038282, Wiley Online Library on [17/07/2025]. See the Terms and Conditions (https://onlinelibrary.wiley.com/doi/10.1029/2024WR038282, Wiley Online Library on [17/07/2025]. See the Terms and Conditions (https://onlinelibrary.wiley.com/doi/10.1029/2024WR038282, Wiley Online Library on [17/07/2025]. See the Terms and Conditions (https://onlinelibrary.wiley.com/doi/10.1029/2024WR038282, Wiley Online Library on [17/07/2025]. See the Terms and Conditions (https://onlinelibrary.wiley.com/doi/10.1029/2024WR038282, Wiley Online Library on [17/07/2025]. See the Terms and Conditions (https://onlinelibrary.wiley.com/doi/10.1029/2024WR038282, Wiley Online Library on [17/07/2025]. See the Terms and Conditions (https://onlinelibrary.wiley.com/doi/10.1029/2024WR038282, Wiley Online Library on [17/07/2025]. See the Terms and Conditions (https://onlinelibrary.wiley.com/doi/10.1029/2024WR038282, Wiley Online Library.wiley.com/doi/10.1029/2024WR038282, Wiley Online Library.wiley.wiley.com/doi/10.1029/2024WR038282, Wiley Online Library.wiley.w

on Wiley Online Library for rules of use; OA articles are governed by the

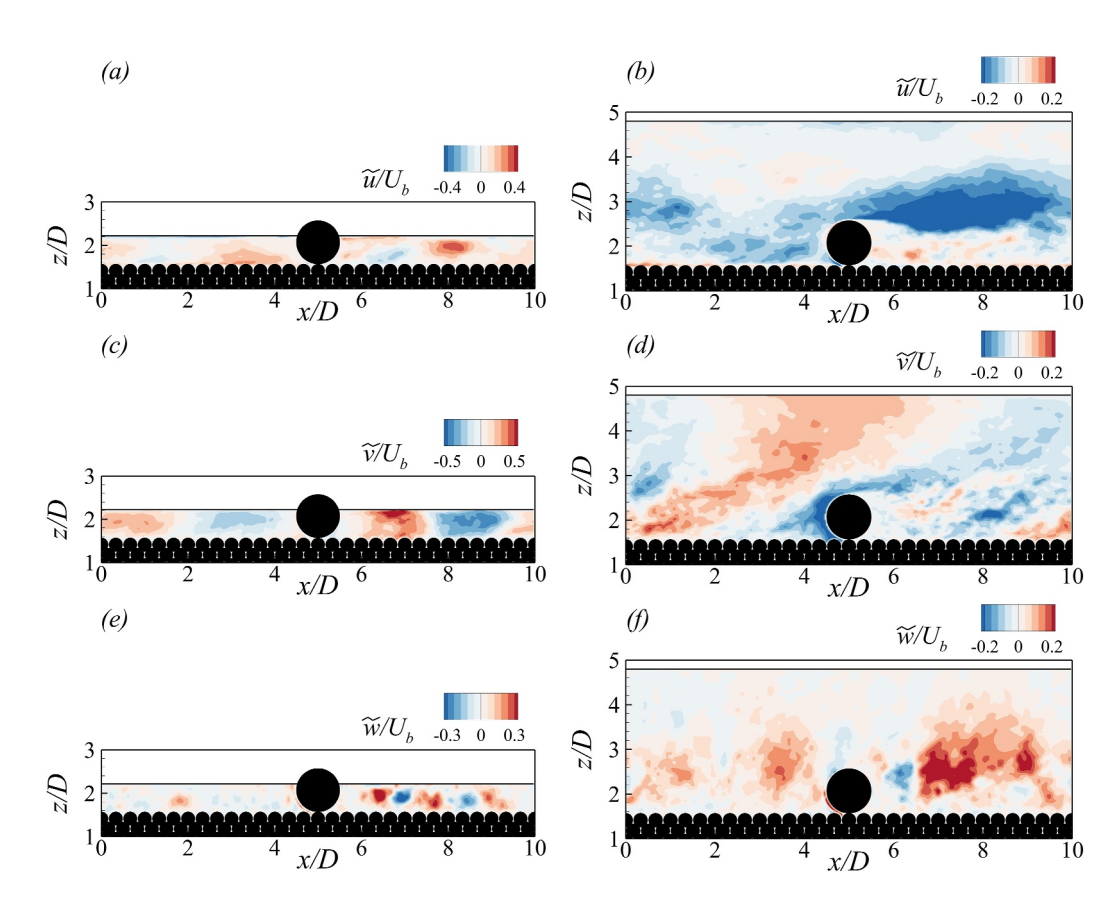


Figure 10. The reconstructed streamwise (a, b), spanwise (c, d), and vertical (e, f) velocity fluctuation fields using the first six proper orthogonal decomposition modes in the symmetry plane at k = 0.75 (left column) and k = 3.5 (right column).

connectance. However, it is evidenced later in Figure 11 that these wavelengths correspond to the flapping of boulder wakes with the constrain of high-speed flow at both sides of boulders.

Finally, at k = 3.5, the $\lambda = 10D$ peak is detected at all three x/D locations in both the symmetry plane (Figure 8e) and the side plane (Figure 9e). This $\lambda = 10D$ peak also emerges at x/D = 0.5 at k = 2.0 (Figure 8d). Two hypotheses are proposed for this wavelength: (a) the streamwise flapping of boulder wakes, analogous to those commonly reported in flow over backward-facing steps (Luo et al., 2023a, 2023c), and (b) the meandering of low-or high-speed streaks recently identified in flow over streamwise-aligned strips (Luo et al., 2023b). Both structures were found to feature large wavelengths on the order of 10 times the height of steps (Luo et al., 2023a, 2023c) or the spanwise spacing of strips (Luo et al., 2023b). These two hypotheses are further verified through the methods of proper orthogonal decomposition (POD) and phase averaging.

POD is capable of separating large-scale turbulence structures from small-scale turbulence, providing insights into the dominant patterns of turbulent motion (Liu et al., 2022a). This procedure involves identifying modes that contain the majority of the TKE and the reconstructed flow fields of the first (few) modes hence contain the most energy. Readers are referred to Liu et al. (2022a) for details of this method. In total, 100 reconstructed velocity instances are obtained in the symmetry plane and in the horizontal plane of $z_1/D = 0.2$, respectively.

Figure 10 presents contours of the reconstructed streamwise (a, b), spanwise (c, d), and vertical (e, f) velocity fluctuations using the first six modes at k = 0.75 (left column) and k = 3.5 (right column). The reconstructed velocity fluctuations at k = 0.25, and 1.25 (Figures S1 and S2 in Supporting Information S1) exhibit similarities to those at k = 0.75, thus are not provided here for brivety. At k = 0.75, the most prominent structures are the alternating distribution of positive and negative spanwise velocities in the streamwise direction. The positive or negative \tilde{v} region occupies an area of approximately 2.1D, supporting the hypothesis that the k = 2.1D peak in Figure 8b represents the lateral flapping of boulder wakes. At k = 3.5, the dominate large-scale flow structures are the brands of negative (Figure 11a) or positive (Movie S1) reconstructed streamwise velocities all along the

TANG ET AL. 14 of 25

1944 7973, 2025, 6, Downloaded from https://agupubs.onlinelibrary.wiley.com/doi/10.1029/2024WR038282, Wiley Online Library on [17/07/2025]. See the Terms and Conditions (https://onlinelibrary.wiley.com/doi/10.1029/2024WR038282, Wiley Online Library on [17/07/2025]. See the Terms and Conditions (https://onlinelibrary.wiley.com/doi/10.1029/2024WR038282).

and-conditions) on Wiley Online Library for rules of use; OA articles are governed by the applicable Creative Commons Licenso

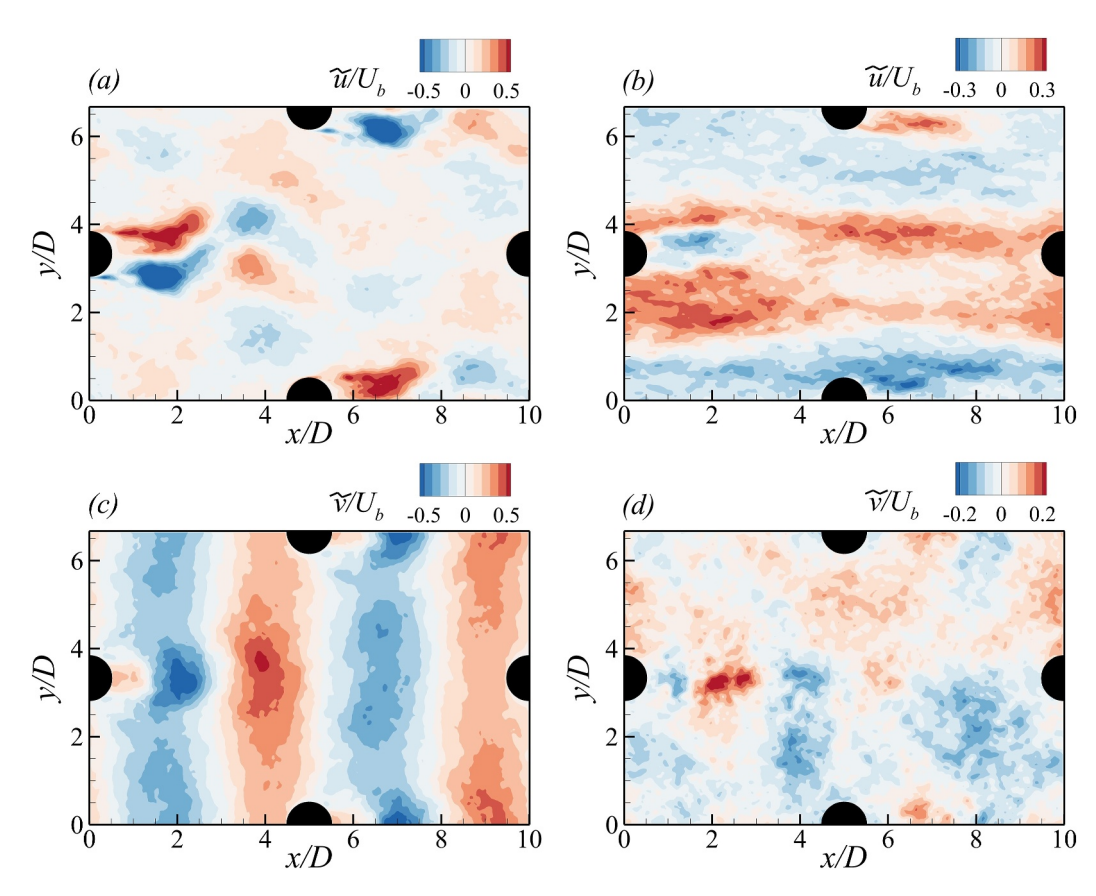


Figure 11. The reconstructed streamwise (a, b) and spanwise (c, d) velocity fluctuation fields using the first six proper orthogonal decomposition modes in the horizontal plane, $z_i/D = 0.2$, at k = 0.75 (left column) and k = 3.5 (right column).

streamwise direction at the elevation near boulder crest. These 10D brands are accompanied by positive (Figure 10f) or negative (Movie S1) reconstructed vertical velocities occupying almost the whole symmetry plane, except for in the wake where a small area of opposite-signed \tilde{w} field occurs. In addition, tilting strips of \tilde{v} (Figure 10d) are observed, originating from the bed surface toward the water surface in a mild angle (~25°).

The reconstructed streamwise (a, b) and spanwise (c, d) velocity fluctuation fields in the horizontal plane, $z_{l}/D = 0.2$, is presented in Figure 11, giving more evidences of the lateral flapping of boulder wakes at k = 0.75. Alternating positive and negative streamwise velocities manifest at the junctures of the shedding flow of high and low velocity, indicating the regularity and intensity of the flapping and its frequency. Also present are patches of stronger spanwise velocity suggesting the presence of vortices, previously shed from the boulder. For k = 3.5, the most distinct large-scale structures are the meandering of the high- and low-speed streaks at the sides of adjacent boulders, respectively (Figure 11b and Movie S2). These streaks span the entire domain length (10D), corroborating what was inferred from Figures 8 and 9. At the spanwise locations of the high-speed streaks, that is, $y/D \approx 2$ and $y/D \approx 4$ in Figure 11b, the reconstructed spanwise velocity (Figure 11d) maintains negative or positive, respectively, indicating separating flow from the symmetry plane to both sides in this horizontal plane. Between the two high-speed streaks, a distinct boulder wake with a wavelength of approximately 4D is observed (Figure 11b). This wake is characterized by an alternating distribution of positive and negative spanwise velocity (Figure 11d) within 4D downstream of the boulders in the symmetry plane. These findings indicate that lateral flapping of boulder wakes persists at k = 3.5, though it is confined to the symmetry plane by the high-speed side streaks. This phenomenon explains the appearance of 4D peaks in the symmetry plane at k = 2.0 and k = 3.5 (Figures 8d and 8e) and the absence of corresponding double-wavelength peaks in the side plane (Figures 9d and 9e) at these submergence levels.

In order to further clarify the origin of these low- and high-speed streaks, a phase-averaging procedure is applied to the velocities in the symmetry plane and the horizontal plane of $z_I/D = 0.2$. This procedure involves (a)

TANG ET AL. 15 of 25

19447973, 2025, 6, Downloaded from https://agupubs.onlinelibrary.wiley.com/doi/10.1029/2024WR038282, Wiley Online Library on [17/07/2025]. See the Terms

-conditions) on Wiley Online Library for rules of use; OA articles

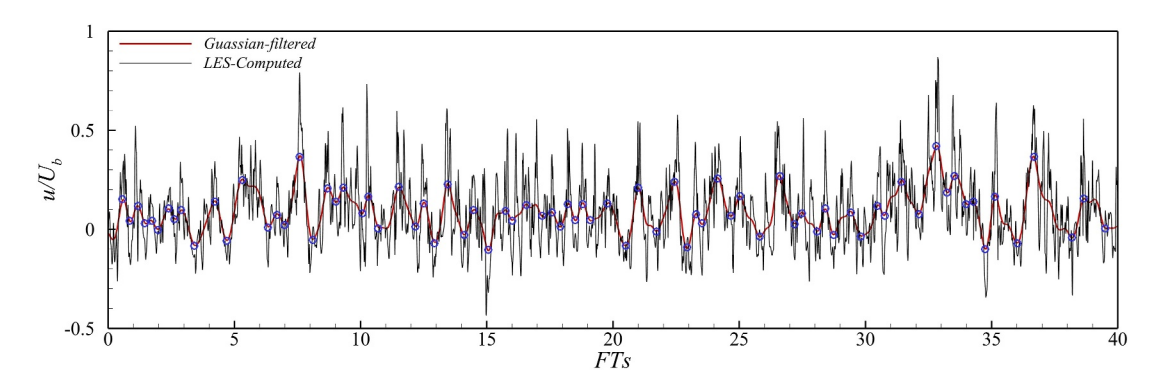


Figure 12. The LES-computed velocity signal and the same signal reconstructed using a Gaussian filter at the symmetric plane x = 2.0D of the boulder.

retaining the turbulence structure of $\lambda = 10D$ by applying a Gaussian filter to the streamwise velocity at x/D = 2.0 and y/D = 3.83 (the red line in Figure 12 represents the filtered velocity signal), then (b) finding the local maxima and minima of the filtered velocity signal (blue hollow circles in Figure 12), and finally (c) calculating the respective average velocities in the symmetry plane and the horizontal plane of $z_1/D = 0.2$ at these maxima and minima. A total of 39 local maxima and minima are identified during the 40 FTs duration data, yielding a periodicity of $\Delta t * U_b/D = 10.2$ (in other words $\lambda = 10.2D$).

Figure 13 presents the phase-averaged streamwise (a, c) and vertical velocities (b, d) in the symmetry plane for the maxima period and the minima period, along with two iso-lines of the phase-averaged (black lines) and the ensemble-averaged (green lines) velocities. The length of the boulder wake exhibits resembles shapes between the maximum (Figure 13a) and the minimum (Figure 13d) periods, both resemble the ensemble-averaged wake shape, particular near the boulder crest. The wake lengths, defined as the distance from the iso-line of $\overline{u}/U_b = 0$ to the boulder center (x = 5D), maintain constant of approximately 2.0D in the two periods. The vertical velocity in these two periods shows little discrepancies as well. These observations demonstrate the absence of the streamwise flapping of boulder wakes.

Distributions of the phase-averaged velocities in the horizontal plane of $z_i/D=0.2$ are presented in Figure 14, along with the iso-lines of the phase-averaged and ensemble-averaged quantities. Figures 14b and 14d clearly demonstrates that lateral flapping occurs in the far wake regions, that is, >2D downstream of the boulder, with alterative distributions of higher-elevated and larger-area spanwise velocity at one side and vice verses at the other side. While the boulder wake, identified by the isoline of $\overline{u}/U_b=0$, is relatively stable in the two phases with limited spanwise flapping at the tails near x/D=2.0, a significant meandering feature is observed for the boundary of the isoline of $\overline{u}/U_b=0.9$ at the both sides of boulders. In summary, the phase-averaged velocity fields (Figures 13 and 14) support the hypothesis of $\lambda=10D$ at k=3.5 corresponding to the meandering of low- or high-speed streaks at both sides of boulders, other than the streamwise flapping of boulder wakes.

4. Discussions

4.1. Classifications of the Flow Regime at Different k

Based on the time-averaged flow and turbulence, the five simulations can be classified into three flow regimes: a low relative submergence (LRS) regime at k = 0.25, an IRS regime at k = 0.75 and 1.25, and a HRS regime at k = 2.0 and 3.5. This classification does not satisfy the criterion proposed by Shamloo et al. (2001), who argued that four flow regimes exit: regime 1 (k < 1), regime 2 (1 < k < 1.3), regime 3 (1.3 < k < 4), and regime 4 (k > 4), or the criterion proposed by Papanicolaou et al. (2018) of regimes 1, 2, and 3 corresponding to k < 1, 1 < k < 3, and k > 3, respectively.

Flow and turbulence in Cases 2 and 3 share many similarities, including the shapes of the boulder wakes and the locations of the "velocity dip" (Figure 3), the distribution of the TKE (Figure 6), and the shape and concentration of CS (Figure 7). All these above features are generated by the dominance of the lateral flapping of boulder wakes (Figure 8) in the intermittent relative submergence. Utilizing the wavelength of the lateral flapping of boulder wakes at the side plane (Figure 9), the Strouhal number, defined as $S_t = fD/U_b = D/\lambda$, is from 0.18 to 0.24. These values are within the range of $S_t = 0.14 \sim 0.24$ reported in literature for wake structures of wall-mounted

TANG ET AL. 16 of 25

19447973, 2025, 6, Downloaded from https://agupubs.onlinelibrary.wiley.com/doi/10.1029/2024WR038282, Wiley Online Library on [17/07/2025]. See the Terms and Conditions (https://onlinelibrary.wiley.com/doi/10.1029/2024WR038282, Wiley Online Library on [17/07/2025]. See the Terms and Conditions (https://onlinelibrary.wiley.com/doi/10.1029/2024WR038282, Wiley Online Library on [17/07/2025]. See the Terms and Conditions (https://onlinelibrary.wiley.com/doi/10.1029/2024WR038282, Wiley Online Library on [17/07/2025]. See the Terms and Conditions (https://onlinelibrary.wiley.com/doi/10.1029/2024WR038282, Wiley Online Library on [17/07/2025]. See the Terms and Conditions (https://onlinelibrary.wiley.com/doi/10.1029/2024WR038282, Wiley Online Library on [17/07/2025]. See the Terms and Conditions (https://onlinelibrary.wiley.com/doi/10.1029/2024WR038282, Wiley Online Library on [17/07/2025]. See the Terms and Conditions (https://onlinelibrary.wiley.com/doi/10.1029/2024WR038282, Wiley Online Library on [17/07/2025]. See the Terms and Conditions (https://onlinelibrary.wiley.com/doi/10.1029/2024WR038282, Wiley Online Library on [17/07/2025]. See the Terms and Conditions (https://onlinelibrary.wiley.com/doi/10.1029/2024WR038282, Wiley Online Library on [17/07/2025]. See the Terms and Conditions (https://onlinelibrary.wiley.com/doi/10.1029/2024WR038282, Wiley Online Library on [17/07/2025]. See the Terms and Conditions (https://onlinelibrary.wiley.com/doi/10.1029/2024WR038282, Wiley Online Library.wiley.com/doi/10.1029/2024WR038282, Wiley Online Library.wiley.wiley.com/doi/10.1029/2024WR038282, Wiley Online Library.wiley.wiley.wiley.wiley.wiley.wiley.wiley.wiley.wiley.wiley.wiley.wiley.wile

conditions) on Wiley Online Library for rules of use; OA article

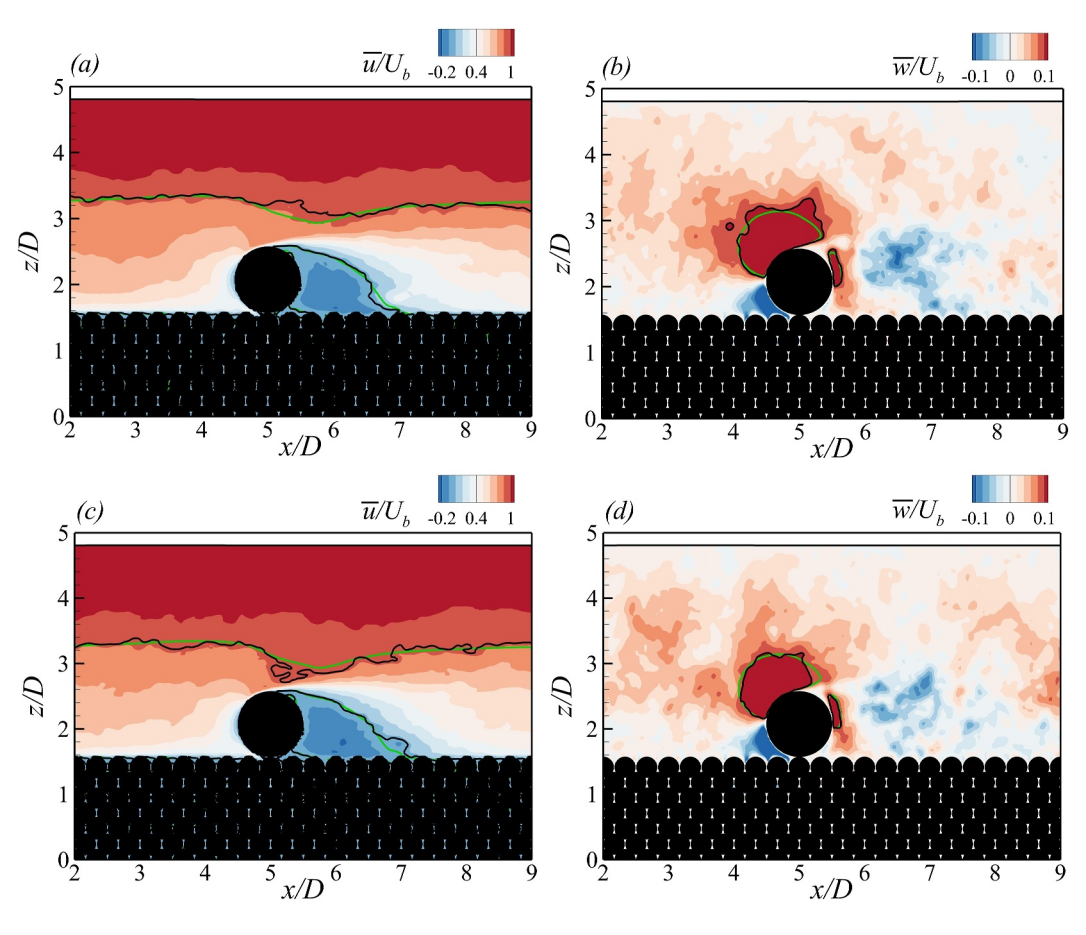


Figure 13. Distributions of phase-averaged streamwise (a, c) and vertical velocities (b, d) deduced from Gaussian-filtered velocity signals in the symmetry plane at k = 3.5. Where (a) and (b) represent the phase-averaged quantities during the maxima period, and (c) and (d) represent those quantities of the minima period. The green lines represent several iso-lines of the ensemble-averaged velocities $\overline{U}/U_b = 0$ and 0.9 in panels (a) and (c), and $\overline{W}/U_b = 0.1$ in panels (b) and (d).

spheres (Hajimirzaie & Buchholz, 2013; Hajimirzaie et al., 2014; Lacey & Rennie, 2012). The current simulations suggest a lower bound of the flow regime 2 (k > 0.75) than that in Shamloo et al.'s (2001) and Papanicolaou et al.'s (2018) classification (k > 1). In addition, flow and turbulence in the Case 1 demonstrates remarkable difference to Cases 2 and 3 in terms of the distributions of time-averaged velocities, TKE, and CS, which demonstrates k = 0.25 as a distinct flow regime (regime 1).

In the HRS regime (k = 2.0 and 3.5), the current LES closely aligns with previous experimental observations (Hajimirzaie et al., 2014) and numerical results (Liu et al., 2017). The flow recirculation length is approximately 2.0D, fitting within the range observed in other studies involving wall-mounted spheres. For example, Ozgoren et al. (2013) and Hajimirzaie et al. (2014) reported recirculation lengths of 1.42D, and 1.90D, respectively. The shape of the funnel vortex in the boulder wake resembles that observed by Liu et al. (2017) for the same k, albeit at a Reynolds number 1.6 times higher. Through the methods of POD and phase averaging, the $\lambda = 10D$ structures in flow over boulder arrays in the HRS regime have been elucidated for the first time, corresponding to the meandering of high-speed streaks at both sides of boulders. Notably, the 10D wavelength matches the length of the computational domain. To eliminate the possibility that this wavelength is an artifact of the domain size constraint, an additional simulation is conducted with a computational domain length of 20D. In this case, the bottom boundary contains only one layer of smaller spheres at k = 3.5. The pre-multiplied spectra at the same locations as those in Figures 8 and 9 are plotted in Figure S3 in Supporting Information S1. As shown in Figure S3 in Supporting Information S1, the 10D wavelength peak remains prominent in the 20D domain, particularly in the side plane. This observation indicates that the meandering of high-speed streaks around the boulders is not constrained by the computational domain length but is instead governed by the streamwise spacing of the

TANG ET AL. 17 of 25

1944 7973, 2025, 6, Downloaded from https://agupubs.onlinelibrary.wiley.com/doi/10.1029/2024WR038282, Wiley Online Library on [17/07/2025]. See the Terms and Conditions (https://onlinelibrary.wiley.com/doi/10.1029/2024WR038282, Wiley Online Library on [17/07/2025]. See the Terms and Conditions (https://onlinelibrary.wiley.com/doi/10.1029/2024WR038282).

tions) on Wiley Online Library for rules of use; OA articles are governed by the applicable Creative Comm

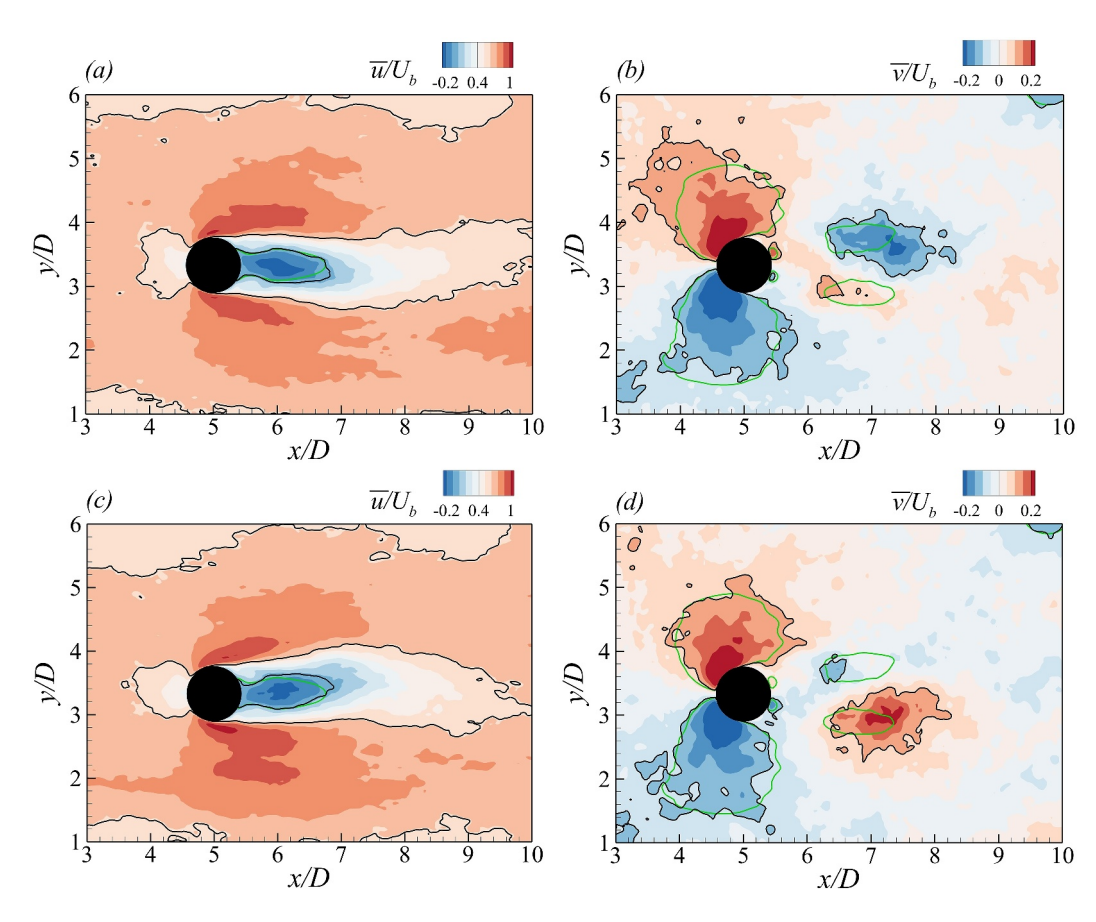


Figure 14. Distributions of phase-averaged streamwise (a, c) and spanwise velocities (b, d) deduced from Gaussian-filtered velocity signals in the horizontal plane of $z_I/D = 0.2$ at k = 3.5. Where (a) and (b) represent the phase-averaged quantities during the maxima period, and (c) and (d) represent those quantities of the minima period. The green lines represent several iso-lines of the ensemble-averaged velocities $\overline{U}/U_b = 0$ and 0.9 in panels (a) and (c), and $\overline{V}/U_b = 0.1$ and -0.1 in panels (b) and (d).

boulders. This meandering pattern mirrors the behavior of high- and low-speed streaks generated by secondary flow instability over streamwise-aligned strips (Luo et al., 2023b) and in partially filled pipes (Liu et al., 2022a).

Current simulation results indicate that the boundary between the LRS and IRS regimes is estimated to lie within the range of k = 0.25–0.75, while the IRS-HRS transition likely occurs between k = 1.25–2.0. However, further systematic investigations combining numerical simulations and experimental validation are recommended to accurately determine the critical thresholds between these three regimes, particularly when accounting for variations in flow velocities and boulder spacing.

4.2. Implications to Sediment Transport

The current simulations provide insights into the turbulence structures at different k, which could be used to further explain the experimental findings on sediment transport through boulder arrays. For example, Papanicolaou et al. (2018) observed the deposition of sediment particles in the boulder wake at k=3.5, whereas at k=0.8, sediment particles accumulated upstream of boulders (Figures 15c and 15f). To explain this distinct deposition patterns, the RSS at $z_1=5$ mm above the riverbed is presented in Figure 15 (the RSS at k=2.0 is presented in Figure S4 in Supporting Information S1). The RSS in the boulder corridor is relatively higher than in other regions for all cases, especially at the two lateral sides of the boulder wake, where high-speed streamwise velocities are observed (Figure 4). In contrast, the RSS in the boulder wake (x/D < 2) is relatively low for all cases due to the low streamwise velocities (Figure 3). It is noteworthy that the low RSS region in the boulder wake expands downstream until approximately x/D=6 (Figure 15e) at k=3.5, whereas at k=0.75 (Figure 15b),

TANG ET AL. 18 of 25

19447973, 2025, 6, Downloaded from https://agupubs.onlinelibrary.wiley.com/doi/10.1029/2024WR038282, Wiley Online Library on [17/07/2025]. See the Terms

are governed by the applicable Creative Commons License

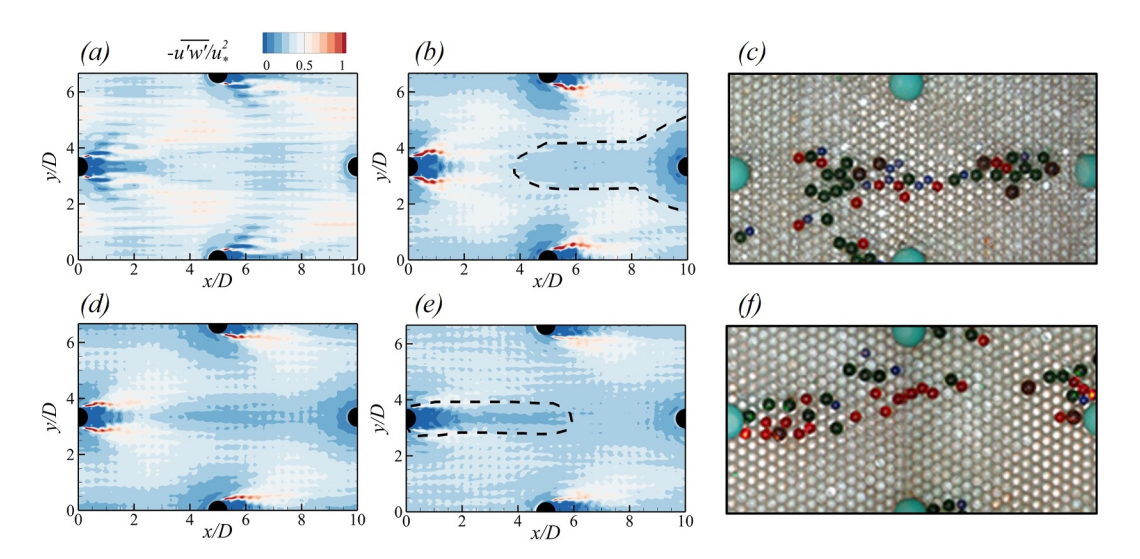


Figure 15. Contours of the Reynolds shear stress at $z_1 = 5$ mm above the bed surface for the four cases (Case 1 (a), Case 2 (b), Case 3 (d), Case 5 (e)). (c) and (f) are the plan view images of the deposited spheres in the experiments from Papanicolaou et al. (2018) of flow through boulder arrays at k = 0.8 and k = 3.5, respectively.

elevated RSS occupies the region of x/D = 2 to 4 and a second low-RSS region (highlighted by the dashed lines) exists upstream of the boulder.

The locations of these low-RSS regions at different k align well with the deposition patterns observed in Papanicolaou et al.'s experiment (2018) as shown in Figures 15c and 15f. Thus, the deposition mechanics of sediment particles at different k is explained as follows: at k = 0.8, the flapping of boulder wakes generates strong spanwise velocities from x/D = 2.0 onwards (Figure 10), resulting in lateral movement of sediment particles toward the symmetry plane. While the elevated TKE (Figure 6b) and RSS (Figure 15b) near x/D = 2.0 supply the energy required for sediment transport, sediments deposits upstream of the downstream boulders, where the spanwise velocity (Figure 10), TKE (Figure 6b), and RSS (Figure 15b) are relatively low. In contrast at k = 3.5, sediment particles are entrained by the funnel vortex in the lee of boulders (Figure 5), and subsequently accumulate in the boulder wake, where both the TKE (Figure 6) and RSS (Figure 15e) are relatively low and flow recirculation occurs (Figure 3).

Papanicolaou et al. (2018) reported two periodicities of bedload transport rate in their experiment, one of a largescale periodicity (about $P_{\rm I} = 8-46$ min) and the other of a small-scale periodicity ($P_{\rm S} = 4$ to 6 minutes). They argued that the small-scale periodicity results from congested bedload movement due to reduced conveyance area within the array, while the large-scale periodicity corresponds to bedload releases around boulders due to lowfrequency eddies. To verify these hypothesis, the pre-multiplied co-spectra of u' and w' at $z_1/D = 0.2$ in the symmetry plane are calculated and depicted in Figure 16. Significant contributions from the three turbulence structures to the RSS are observed. At k = 0.25, although the pre-multiplied co-spectra peaks at the wavelength $\lambda = 2.1D$, the relative contribution $(Ps^+(uw))$ is below 2%. At IRS, contributions from the flapping of boulder wakes increase significantly to approximately 20%. At k = 2.0 and 3.5, the primary source of RSS originates from the large-scale meandering of low- and high-speed streaks, accounting for approximately 20% of the near-bed RSS. Notably, the ratio of wavelengths of the meandering of low- and high-speed streaks and the flapping of boulder wakes is 4.8, identical to the ratio of the large-scale periodicity to the small-scale periodicity of the bedload transport rate (4.8 ± 2.8) measured in Papanicolaou et al.'s experiment (2018). This supports Papanicolaou et al.'s (2018) hypothesis that the large-scale bedload periodicity corresponds to bedload releases around boulders due to low-frequency eddies, more precisely the low-frequency meandering of low- and high-speed streaks. Meanwhile, the current LES demonstrates the small-scale bedload periodicity is caused by bedload releases due to the flapping of boulder wakes.

TANG ET AL. 19 of 25

1944/9793, 2025, 6, Downloaded from https://agupubs.onlinelibrary.wiley.com/doi/10.1029/2024WR038282, Wiley Online Library on [17/07/2025]. See the Terms and Conditions (https://onlinelibrary.wiley.com/erms-and-conditions) on Wiley Online Library for rules of use; OA articles are governed by the applicable Creative Commons Licenseagure Commons Licenseagure Commons (https://onlinelibrary.wiley.com/erms-and-conditions) on Wiley Online Library for rules of use; OA articles are governed by the applicable Creative Commons Licenseagure Commons Licenseagure Commons (https://onlinelibrary.wiley.com/erms-and-conditions) on Wiley Online Library for rules of use; OA articles are governed by the applicable Creative Commons Licenseagure Commons Licenseagure Commons (https://onlinelibrary.wiley.com/erms-and-conditions) on Wiley Online Library for rules of use; OA articles are governed by the applicable Creative Commons Licenseagure Commons Licenseagure Commons (https://onlinelibrary.wiley.com/erms-and-conditions) on Wiley Online Library for rules of use; OA articles are governed by the applicable Creative Commons Licenseagure Commons (https://onlinelibrary.wiley.com/erms-and-conditions) on Wiley Online Library for rules of use; OA articles are governed by the applicable Creative Commons Licenseagure Commons Licenseagure Commons (https://onlinelibrary.wiley.com/erms-and-conditions) on Wiley Online Library for rules of use; OA articles are governed by the applicable Creative Commons (https://onlinelibrary.wiley.com/erms-and-conditions) on Wiley Online Library for rules of use; OA articles are governed by the applicable Creative Commons (https://onlinelibrary.wiley.com/erms-and-conditions) on Wiley Online Library for rules of use; OA articles are governed by the applicable Creative Commons (https://onlinelibrary.wiley.com/erms-and-conditions) on the applicable Creative Commons (https://onlinelibrary.wiley.com/erms-and-conditions) on the applicable Creative Commons (https://onlinelibrary.wiley.com/erms-and-conditions) on the app

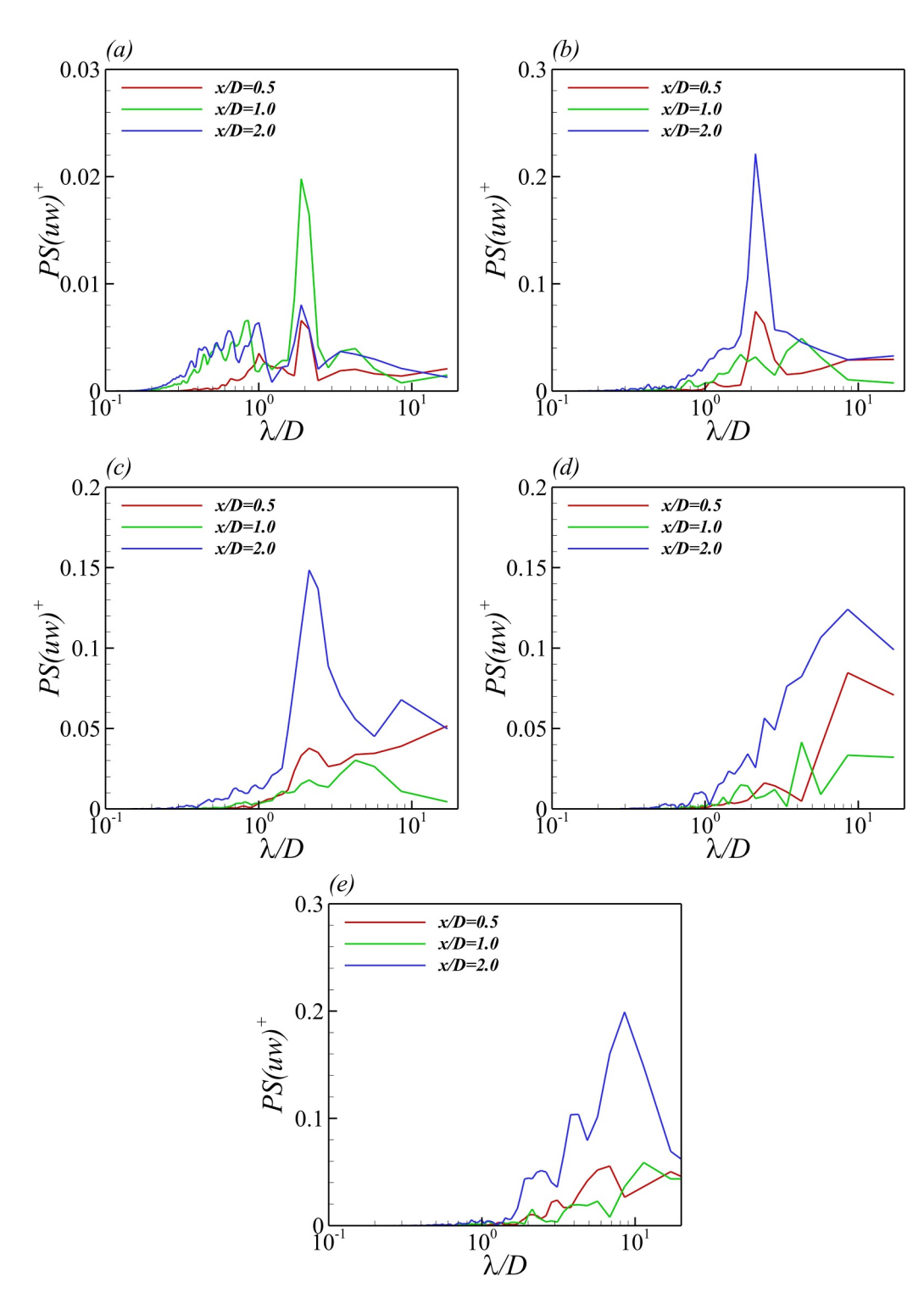


Figure 16. Pre-multiplied co-spectra of fluctuations of the streamwise velocity and the vertical velocity at $z_1/D = 0.20$ in the plane of y/D = 3.33 for Case 1 (a) to Case 5 (e).

4.3. Limitations

In natural river systems, boulders typically exhibit ellipsoidal rather than idealized spherical shapes (Lamb et al., 2017; Strom & Papanicolaou, 2008). Flume experiments comparing drag coefficients between natural cobbles and spherical particles under equivalent relative submergence conditions have shown that non-spherical

TANG ET AL. 20 of 25



particles exhibit drag coefficients comparable to those of spheres (Lamb et al., 2017). Under low submergence conditions, laboratory experiments have consistently shown that sediment accumulates upstream of large obstacles, irrespective of whether the obstacles are spherical (Papanicolaou et al., 2018) or naturally shaped boulders (Polvi, 2021). These observations support the applicability of the flow regime classification and associated turbulence structures proposed in this study to riverbeds containing ellipsoidal boulders. Conversely, boulder spacing emerges as a critical parameter significantly affecting the flow field nearby. The LES employs a constant, relatively large boulder spacing, where there is no interference between boulder wakes, falling within the isolated wake regime (Papanicolaou et al., 2001). According to the classification by Papanicolaou et al. (2001), the wake regimes of a streambed with large boulders can be categorized based on boulder spacing: isolated (spacing > 6.0D), wake interference (spacing = 2.0D), and skimming (spacing = 1.0D). In a previous study investigating the same bed configuration at k = 3.5 (Fang et al., 2017), significant variations in wake structures, near-bed shear stress distribution, and bedload transport rates have been observed across boulder spacings ranging from 2D to 10D. The influence of boulder spacing on turbulence structures and sediment deposition at different k values represents a critical and intriguing area of research. Further investigation is encouraged to determine whether the three distinct turbulence structures mentioned above persist as the boulder spacing decreases.

Given the nature of the IB method, where computational cells are defined around elements without precisely conforming to their surfaces, grid resolution near the elements plays a critical role. This resolution is determined based on the spatially averaged wall-normal distance from the first fluid grid points near the elements ($\langle \Delta r \rangle$) and the local friction velocity, as proposed by Liu et al. (2024). For a uniform computational grid, $\langle \Delta r \rangle$ is approximately half the grid spacing, regardless of the size of the elements. The local friction velocity, $u_{*,bou}$ or $u_{*,sph}$ computed via the gradient of the double-averaged tangential velocity as $\sqrt{\nu \langle \overline{V_p} \rangle / \langle \Delta r \rangle}$, is significantly lower than the reach-averaged friction velocity $u_{*,v}$, which is derived from the reach-averaged pressure gradient. This difference arises because a substantial portion of the reach-averaged flow resistance is due to the form drag of boulders, as demonstrated in both numerical simulations (Liu et al., 2024) and flume experiments (Lamb et al., 2017; Yager et al., 2007). Across Cases 1 to 5, the largest near-element grid resolution (D^+ and d^+) is $D^+ = 6.3$ (Table 1). This resolution satisfies the requirement of having at least one grid point within the viscous sublayer near the boulders, as stipulated by the IB method applied in this study (Uhlmann, 2005). Additionally, it aligns with the grid resolution range reported for partially filled pipe flow $(\Delta x^+ \approx 15, \Delta y^+ = \Delta z^+ \approx 5)$ in Liu et al. (2022b). This consistency supports the grid independence of the results demonstrated in Liu et al. (2017). However, it is important to note that the current near-element resolution is still coarser than the recommended values for smooth-wall-modeled LES ($\Delta z^+ \approx 1$, $\Delta v^+ \approx 20$, $\Delta x^+ \approx 100$) as outlined by Rodi et al. (2013). This discrepancy may lead to reduced accuracy in the near-element regions, particularly in resolving subsurface flow dynamics.

A critical aspect to note is the significantly longer time required for subsurface flow to fully develop under high submergence conditions compared to surface currents. The differences between time-averaged surface and subsurface flow velocities obtained after 10 FTs from short-term statistics and long-term statistics across all simulations are provided in Table S2 in Supporting Information S1. The results indicate that while the difference in surface flow velocity remains below 5% across all simulations, the discrepancy in subsurface flow velocity can reach up to 30% at k = 3.5 (Table S2 in Supporting Information S1). Although the time-averaging process in this study commenced relatively early, the extended duration of statistical collection (90.4FTs) is considered sufficient to minimize its influence on the numerical results. Furthermore, since subsurface flow is not the primary focus of this analysis, its potential impact on the conclusions is deemed negligible. However, these findings underscore the importance of accounting for the prolonged development time of subsurface flow in future studies focusing on such dynamics.

Bedload transport and channel bed deformation are not simulated in the LES. Several experiments (Monsalve & Yager, 2017; Monsalve et al., 2017) have shown that bedload transport rates through boulder arrays vary over an order of magnitude as the erodible beds deform. Therefore, simulations considering fully coupled hydrodynamics and bed deformations are encouraged to provide further insights into the alteration of turbulence structures, bed shear stress, and subsequent bedload transport rates.

TANG ET AL. 21 of 25

19447973, 2025, 6, Downloaded from https://agupubs.onlinelibrary.wiley.com/doi/10.1029/2024WR038282, Wiley Online Library on [17/07/2025]. See the Terms

on Wiley Online Library for rules

are governed by the applicable Creative Commons License

Table 3						
Summary of the	Key	Features	Across	Different	Flow	Regimes

Regimes	LRS	IRS	HRS
Relative Submergence	k = 0.25	$0.75 \le k \le 1.25$	$2.0 \le k \le 3.5$
Locations of the Highest Flow Velocity	Upstream of boulders	Upstream of boulders	Above boulders
Time-Averaged Wake Structures	Subsurface flow ejection	Spanwise flow entrainment	Tornado-shaped flow recirculation
TKE Distributions	Uniform across the entire water depth	Highest downstream of boulder wakes	Highest downstream of boulder crests
Dominant Turbulence Structures	Near-bed hairpin vortices	Flapping of boulder wakes	Meandering of high-speed streaks
Wavelengths of Dominant Turbulence Structures	0.8D	2.1 <i>D</i>	10 <i>D</i>
Potential Sediment Deposition Regions	Upstream of boulders	Upstream of boulders	In boulder wakes

5. Conclusions

Large eddy simulations have been conducted to explore the impact of k on the turbulence structures in flow through boulder arrays. An open-channel bed has been artificially roughened by seven layers of closely packed spheres are equipped with moderately spaced boulders. The LES have been validated first using velocity data published in literature with similar bed configurations. Then the impact of k on the time-averaged flow field and turbulence structures has been visualized and quantified. It is observed that the five simulations can be categorized into three regimes based on k. The key characteristics of each regime, including mean flow statistics, dominant turbulence structures, and their influence on sediment depositions, are summarized in Table 3.

At the LRS regime (k = 0.25), boulder wakes, characterized by recirculation flows, are absent, and the time-averaged flow exhibits two-dimensional characteristics, including low vertical flow velocities, straight streamlines, and uniform TKE throughout the water depth. At the IRS regime (k = 0.75 and 1.25), elevated levels of TKE generated downstream of the boulder wakes. At the HRS regime (k = 2.0 and 3.5), time-averaged funnel vortices are apparent in the wakes, with the most intense TKE generated by the detachment of the shear layer from the crest of boulders.

Three distinct types of CS are identified within the flow through boulder arrays: short-wavelength structures ($\lambda=0.8D$) at the lowest k, intermediate-wavelength structures ($\lambda=2.1D$) at $k \le 1.25$, and long-wavelength structures ($\lambda=10D$) at the $k \ge 2.0$ near the riverbed. Through the Q-criterion, POD, and phase averaging analysis, these structures are identified as the near-bed hairpin vortex, the spanwise flapping of boulder wakes, and the meandering of low- and high-speed streaks at both sides of boulders. These CS contribute up to 20% of the Reynolds shear stress in the wake and influence the distribution of bed shear stress at different k. A region of low bed shear stress occurs upstream of boulders at low k, while it shifts to the wake of boulders at high k, which corresponds to the different deposition patterns observed at different k by Papanicolaou et al. (2018).

Data Availability Statement

The open-source code, Hydro3D (version 7.0) published on Zenodo, and the data are available from Liu et al. (2025).

Notations

D the diameter of boulder [L]

 D^+ the normalized near-boulder grid resolution [–]

d the diameter of sphere [L]

 d^+ the normalized near-sphere grid resolution [-]

TANG ET AL. 22 of 25

1944 7973, 2025, 6, Downloaded from https://agupubs.onlinelibrary.wiley.com/doi/10.1029/2024WR038822, Wiley Online Library on [17/07/2025]. See the Terms and Conditions (https://onlinelibrary.wiley.com/doi/10.1029/2024WR038822, Wiley Online Library on [17/07/2025]. See the Terms and Conditions (https://onlinelibrary.wiley.com/doi/10.1029/2024WR038822).

-and-conditions) on Wiley Online Library for rules of use; OA articles are governed by the applicable Creative Commons Licenso

```
the volume force introduced in the immersed boundary (IB) method [ML<sup>-2</sup>T<sup>-2</sup>]
f_i
Fr
             the Froude number [-]
             the gravitational acceleration [LT<sup>-2</sup>]
g_i
H
             the depth of water [L]
k
             relative submergence [-]
             the length of the x-direction computation domain [L]
L_{x}
             the length of the y-direction computation domain [L]
L_{v}
             the length of the z-direction computation domain [L]
L_z
N_x
             the number of grids in the x direction
N_{v}
             the number of grids in the y direction
N_{z}
             the number of grids in the z direction
             the resolved pressure [ML^{-1}T^{-2}]
p
             the Reynolds number [-]
Re
             the filtered strain-rate tensor [T^{-1}]
S_{ii}
             the turbulent kinetic energy [ML<sup>2</sup>T<sup>-2</sup>]
TKE
             the bulk velocity [LT<sup>-1</sup>]
U_b
             the velocity vector in the i direction [LT<sup>-1</sup>]
u_i
             the velocity vector in the j direction [LT<sup>-1</sup>]
u_i
             the global-averaged friction velocity [LT<sup>-1</sup>]
u_{*,g}
             the friction velocity acting on boulders [LT<sup>-1</sup>]
u_{*,bou}
             the friction velocity acting on spheres [LT<sup>-1</sup>]
u_{*,sph}
V_{p}
             the tangential velocity at the first fluid node near boulders or spheres [LT<sup>-1</sup>]
             the spatial vectors in the three directions [L]
x_i
             the vertical distance above the riverbed [L]
z_1
             the height of riverbed [L]
z_{bed}
             the air-phase domain [L<sup>3</sup>]
\Omega_{gas}
             the water-phase domain [L<sup>3</sup>]
\Omega_{liguid}
             the sub-grid scale (SGS) stress [ML<sup>-1</sup>T<sup>-2</sup>]
	au_{ij}
λ
             wavelength [L]
             the kinematic viscosity [L^2T^{-1}]
             water density [ML<sup>-3</sup>]
ρ
             the normal distance from the first fluid node to the surface of boulders or spheres [L]
\Delta r
```

TANG ET AL. 23 of 25

19447973, 2025, 6, Downloaded from https://agupubs.onlinelibrary.wiley.com/doi/10.1029/2024WR038282, Wiley Online Library on [17/07/2025]. See the Terms

on Wiley Online Library for rules of use; OA articles

are governed by the applicable Creative Commons

Acknowledgments

Financial support for this work is provided by the National Key Research and Development Project (2022YFC3201802), the National Natural Science Foundation of China (12372383), Shenzhen Science and Technology Program (JCYJ20230807093507015) and the Highlevel University Special Fund (G03050K001). The authors would like to acknowledge the support of the highperformance cluster centers "Taiyi" of the Southern University of Science and Technology.

References

- Baki, A. B., Zhu, D. Z., & Rajaratnam, N. (2016). Flow simulation in a rock-ramp fish pass. *Journal of Hydraulic Engineering*, 142(10), 04016031. https://doi.org/10.1061/(ASCE)HY.1943-7900.0001166
- Bathurst, J. C. (1987). Critical conditions for bed material movement in steep, boulder-bed streams (pp. 309–318). IAHS-AISH publication. Bathurst, J. C. (2002). At-a-site variation and minimum flow resistance for mountain rivers. Journal of Hydrology, 269(1–2), 11–26. https://doi.org/10.1016/S0022-1694(02)00191-9
- Best, J. L. (2001). Visualisation of coherent flow structures associated with particle clusters: Temporal and spatial characterisation revealed using ultrasonic Doppler velocity profiling. *Gravel-Bed Rivers* 2000 CD-ROM.
- Dey, S., Sarkar, S., Bose, S. K., Tait, S. J., & Castro-Orgaz, O. (2011). Wall-wake flows downstream of a sphere placed on a plane rough wall. Journal of Hydraulic Engineering, 137(10), 1173–1189. https://doi.org/10.1061/(ASCE)HY.1943-7900.0000441
- Duan, Y., Zhong, Q., Wang, G., Zhang, P., & Li, D. (2021). Contributions of different scales of turbulent motions to the mean wall-shear stress in open channel flows at low-to-moderate Reynolds numbers. *Journal of Fluid Mechanics*, 918, A40. https://doi.org/10.1017/jfm.2021.236
- Dudunake, T. J., Tonina, D., Reeder, W. J., & Monsalve, A. (2020). Local and reach-scale hyporheic flow response from Boulder-Induced geomorphic changes. Water Resources Research, 56(10). https://doi.org/10.1029/2020WR027719
- Fang, H., Liu, Y., & Stoesser, T. (2017). Influence of Boulder concentration on turbulence and sediment transport in open-channel flow over submerged boulders. *Journal of Geophysical Research: Earth Surface*, 122(12), 2392–2410. https://doi.org/10.1002/2017JF004221
- Ferro, V. (2003). ADV measurements of velocity distributions in a gravel-bed flume. Earth Surface Processes and Landforms, 28(7), 707–722. https://doi.org/10.1002/esp.467
- Golpira, A., Baki, A. B., Ghamry, H. K., & Katopodis, C. (2023). Influence of boulder submergence ratio on local flow field: Implications for
- sediment and fish instream habitat. Ecological Engineering, 193, 106997. https://doi.org/10.1016/j.ecoleng.2023.106997
 Hajimirzaie, S. M., & Buchholz, J. H. (2013). Flow dynamics in the wakes of low-aspect-ratio wall-mounted obstacles. Experiments in Fluids,
- 54(11), 1–14. https://doi.org/10.1007/s00348-013-1616-1
 Hajimirzaie, S. M., Tsakiris, A. G., Buchholz, J. H., & Papanicolaou, A. N. (2014). Flow characteristics around a wall-mounted spherical obstacle
- in a thin boundary layer. Experiments in Fluids, 55(6), 1–14. https://doi.org/10.1007/s00348-014-1762-0
- Hajimirzaie, S. M., Wojcik, C. J., & Buchholz, J. H. (2012). The role of shape and relative submergence on the structure of wakes of low-aspect-ratio wall-mounted bodies. *Experiments in Fluids*, 53(6), 1943–1962. https://doi.org/10.1007/s00348-012-1406-1
- Hunt, J. C., Wray, A. A., & Moin, P. (1988). Eddies, streams, and convergence zones in turbulent flows. Studying turbulence using numerical simulation databases, 2. In Proceedings of the 1988 summer program.
- Kang, S., Lightbody, A. F., Hill, C., & Sotiropoulos, F. (2011). High-resolution numerical simulation of turbulence in natural waterways. Advances in Water Resources, 34(1), 98–113. https://doi.org/10.1016/j.advwatres.2010.09.018
- Kramer, C. M., & Papanicolaou, A. N. (2012). The effects of relative submergence on cluster formation in gravel bed streams. In *Impacts of global climate change* (pp. 1–12). https://doi.org/10.1061/40792(173)579
- Lacey, R. J., & Rennie, C. D. (2012). Laboratory investigation of turbulent flow structure around a bed-mounted cube at multiple flow stages. Journal of Hydraulic Engineering, 138(1), 71–84. https://doi.org/10.1061/(ASCE)HY.1943-7900.0000476
- Lacey, R. W., & Roy, A. G. (2008). Fine-scale characterization of the turbulent shear layer of an instream pebble cluster. *Journal of Hydraulic*
- Engineering, 134(7), 925–936. https://doi.org/10.1061/(ASCE)0733-9429(2008)134:7(925)

 Lamb, M. P., Brun, F., & Fuller, B. M. (2017). Direct measurements of lift and drag on shallowly submerged cobbles in steep streams: Implications for flow resistance and sediment transport. Water Resources Research, 53(9), 7607–7629. https://doi.org/10.1002/2017WR020883
- Lee, A., Aubeneau, A. F., Cardenas, M. B., & Liu, X. (2022). Hyporheic exchange due to cobbles on sandy beds. Water Resources Research, 58(1). https://doi.org/10.1029/2021WR030164
- Liu, Y., Reible, D. D., Hussain, F., & Fang, H. (2019). Role of bioroughness, bioirrigation, and turbulence on oxygen dynamics at the sediment-water interface. Water Resources Research, 55(10), 8061–8075. https://doi.org/10.1029/2019WR025098
- Liu, Y., Stoesser, T., & Fang, H. (2022a). Impact of turbulence and secondary flow on the water surface in partially filled pipes. *Physics of Fluids*, 34(3), https://doi.org/10.1063/5.0078564
- Liu, Y., Stoesser, T., & Fang, H. (2022b). Effect of secondary currents on the flow and turbulence in partially filled pipes. *Journal of Fluid Mechanics*, 938, A16. https://doi.org/10.1017/jfm.2022.141
- Liu, Y., Stoesser, T., Fang, H., Papanicolaou, A. N., & Tsakiris, A. G. (2017). Turbulent flow over an array of boulders placed on a rough, permeable bed. Computers & Fluids, 158, 120–132. https://doi.org/10.1016/j.compfluid.2017.05.023
- Liu, Y., Tang, Z., Huang, L., Stoesser, T., & Fang, H. (2024). On the role of the Froude number on flow, turbulence, and hyporheic exchange in open-channel flow through boulder arrays. *Physics of Fluids*, 36(9). https://doi.org/10.1063/5.0222673
- Liu, Y., Tang, Z., & Stoesser, T. (2025). The software and input files for the WRR paper Impact of the relative submergence on turbulence structures in open-channel flow through arrays of large spherical roughness elements [Software] [Dataset]. Zenodo. https://doi.org/10.5281/ zenodo.14590622
- Luo, Q., Dolcetti, G., Stoesser, T., & Tait, S. (2023a). Water surface response to turbulent flow over a backward-facing step. *Journal of Fluid Mechanics*, 966, A18. https://doi.org/10.1017/jfm.2023.350
- Luo, Q., Stoesser, T., Cameron, S., Nikora, V., Zampiron, A., & Patella, W. (2023b). Meandering of instantaneous large-scale structures in open-channel flow over longitudinal ridges. *Environmental Fluid Mechanics*, 23(4), 829–846. https://doi.org/10.1007/s10652-023-09934-0
- Luo, Q., Stoesser, T., Jalalabadi, R., & Xie, Z. (2023c). Hydrodynamics and turbulence of free-surface flow over a backward-facing step. *Journal of Hydraulic Research*, 61(5), 611–630. https://doi.org/10.1080/00221686.2023.2239751
- Monsalve, A., & Yager, E. M. (2017). Bed surface adjustments to spatially variable flow in low relative submergence regimes. *Water Resources Research*, 53(11), 9350–9367. https://doi.org/10.1002/2017WR020845
- Monsalve, A., Yager, E. M., & Schmeeckle, M. W. (2017). Effects of bed forms and large protruding grains on near-bed flow hydraulics in low relative submergence conditions. *Journal of Geophysical Research: Earth Surface*, 122(10), 1845–1866. https://doi.org/10.1002/ 2016JF004152
- Montgomery, D. R., & Buffington, J. M. (1997). Channel-reach morphology in mountain drainage basins. *Geological Society of America Bulletin*, 109(5), 596–611. https://doi.org/10.1130/0016-7606(1997)109<0596:CRMIMD>2.3.CO;2
- Nativ, R., Turowski, J. M., Goren, L., Laronne, J. B., & Shyu, J. B. (2022). Influence of rarely mobile boulders on channel width and slope: Theory and field application. *Journal of Geophysical Research: Earth Surface*, 127(9). https://doi.org/10.1029/2021JF006537
- Nicoud, F., & Ducros, F. (1999). Subgrid-scale stress modelling based on the square of the velocity gradient tensor. Flow, Turbulence and Combustion, 62(3), 183–200. https://doi.org/10.1023/A:1009995426001

TANG ET AL. 24 of 25



Water Resources Research

- 10.1029/2024WR038282
- Osher, S. J., & Sethian, J. A. (1988). Fronts propagating with curvature-dependent speed: Algorithms based on Hamilton-Jacobi formulations. *Journal of Computational Physics*, 79(1), 12–49. https://doi.org/10.1016/0021-9991(88)90002-2
- Ouro, P., Fraga, B., López-Novoa, U., & Stoesser, T. (2019). Scalability of an Eulerian-Lagrangian large-eddy simulation solver with hybrid MPI/ OpenMP parallelisation. *Computers & Fluids*, 179, 123–136. https://doi.org/10.1016/j.compfluid.2018.10.013
- Ozgoren, M., Okbaz, A., Dogan, S., Şahin, B., & Akilli, H. (2013). Investigation of flow characteristics around a sphere placed in a boundary layer over a flat plate. Experimental Thermal and Fluid Science, 44, 62–74. https://doi.org/10.1016/j.expthermflusci.2012.05.014
- Papanicolaou, A. N., Diplas, P., Dancey, C. L., & Balakrishnan, M. (2001). Surface roughness effects in near-bed turbulence: Implications to sediment entrainment. *Journal of Engineering Mechanics*, 127(3), 211–218. https://doi.org/10.1061/(ASCE)0733-9399(2001)127:3(211)
- Papanicolaou, A. N., Kramer, C. M., Tsakiris, A. G., Stoesser, T., Bomminayuni, S. K., & Chen, Z. (2012). Effects of a fully submerged boulder within a boulder array on the mean and turbulent flow fields: Implications to bedload transport. Acta Geophysica, 60(6), 1502–1546. https://doi.org/10.2478/s11600-012-0044-6
- Papanicolaou, A. N., Tsakiris, A. G., Wyssmann, M. A., & Kramer, C. M. (2018). Boulder array effects on bedload pulses and depositional patches. *Journal of Geophysical Research: Earth Surface*, 123(11), 2925–2953. https://doi.org/10.1029/2018JF004753
- Parker, G. (2013). Transport of gravel and sediment mixtures. Sedimentation Engineering, 165–251. https://doi.org/10.1061/9780784408148.ch03
- Polvi, L. E. (2021). Morphodynamics of boulder-bed semi-alluvial streams in northern Fennoscandia: A flume experiment to determine sediment self-organization. Water Resources Research, 57(3), e2020WR028859. https://doi.org/10.1029/2020WR028859
- Rickenmann, D. (2001). Comparison of bed load transport in torrents and gravel bed streams. Water Resources Research, 37(12), 3295–3305. https://doi.org/10.1029/2001WR000319
- Rodi, W., Constantinescu, G., & Stoesser, T. (2013). Large-eddy simulation in hydraulics. https://doi.org/10.1201/b15090
- Shamloo, H., Rajaratnam, N., & Katopodis, C. (2001). Hydraulics of simple habitat structures. *Journal of Hydraulic Research*, 39(4), 351–366. https://doi.org/10.1080/00221680109499840
- Strom, K., & Papanicolaou, A. N. (2007). ADV measurements around a cluster microform in a shallow mountain stream. *Journal of Hydraulic Engineering*, 133(12), 1379–1389. https://doi.org/10.1061/(ASCE)0733-9429(2007)133:12(1379)
- Strom, K., & Papanicolaou, A. N. (2008). Morphological characterization of cluster microforms. Sedimentology, 55(1), 137–153. https://doi.org/10.1111/j.1365-3091.2007.00895.x
- Tokyay, T., & Constantinescu, S. (2006). Validation of a large-eddy simulation model to simulate flow in pump intakes of realistic geometry. Journal of Hydraulic Engineering, 132(12), 1303–1315. https://doi.org/10.1061/(ASCE)0733-9429(2006)132:12(1303)
- Tsakiris, A. G., Papanicolaou, A. N., Hajimirzaie, S. M., & Buchholz, J. H. (2014). Influence of collective boulder array on the surrounding time-averaged and turbulent flow fields. *Journal of Mountain Science*, 11(6), 1420–1428. https://doi.org/10.1007/s11629-014-3055-8
- Uhlmann, M. (2005). An immersed boundary method with direct forcing for the simulation of particulate flows. *Journal of Computational Physics*, 209(2), 448–476. https://doi.org/10.1016/j.jcp.2005.03.017
- Wilcock, P. R., & Crowe, J. C. (2003). Surface-based transport model for mixed-size sediment. *Journal of Hydraulic Engineering*, 129(2), 120–128. https://doi.org/10.1061/(ASCE)0733-9429(2003)129:2(120)
- Yager, E. M., Kirchner, J. W., & Dietrich, W. E. (2007). Calculating bed load transport in steep boulder bed channels. *Water Resources Research*, 43(7). https://doi.org/10.1029/2006WR005432

TANG ET AL. 25 of 25